9-12-2014

Integration of CdSe/ZnS Quantum Dots into As-induced Etched Nanovoids on GaSb

Shayla Nahar Bhuiya

Shayla Nahar Bhuiya
Candidate

Electrical and Computer Engineering
Department

This thesis is approved, and it is acceptable in quality and form for publication:

Approved by the Thesis Committee:

Dr. Ganesh Balakrishnan, Chairperson

Dr. Thomas Rotter

Dr. Ashwin K. Rishinaramangalam

INTEGRATION OF CDSE/ZNS QUANTUM DOTS INTO AS-INDUCED ETCHED NANOVOIDS ON GASB

by

SHAYLA NAHAR BHUIYA

B.S. IN ELECTRONIC AND TELECOMMUNICATION ENGINEERING, NORTH SOUTH UNIVERSITY, DHAKA, BANGLADESH, 2011

THESIS

Submitted in Partial Fulfillment of the
Requirements for the Degree of

Master of Science
Electrical Engineering

The University of New Mexico
Albuquerque, New Mexico

July, 2014

ACKNOWLEDGEMENTS

First and foremost, I would like to thank my parents for all their love and support throughout this endeavor; my Dad, for calling me almost every single day for updates on my education, my day-to-day life, and my Mom, for believing in me, and for comforting me during all those moments when I felt homesick.

I would, also, like to thank Dr. Ganesh Balakrishnan for being my thesis chair. He has been instrumental in guiding me through my research and editing my thesis work. My sincerest gratitude to Dr.Osinski, who introduced me to the world of nano-materials and guided me through some of the experiments required in my research. Gratitude is also extended to Dr. Ashwin Rishinaramangalam and Dr. Thomas Rotter for being my thesis committee members.

I would like to thank my labmates at CHTM for making my experience at work a great one. John Plumley and Brian Akins have been excellent mentors when I started developing my technical skills in the lab. Special thanks to John Plumley for his valuable insights, remarks and discussions throughout the course of my research. Also, thanks to Emma Renteria, Ayse and Orlando for assisting me during those long SEM sessions. Thanks to Antonio, Tasha, and Nathan for insights and suggestions, and Leisha for being such a sweetheart. Her intellect, witty nature, and positive outlook, even during stressful times, have been very encouraging. I would also like to acknowledge my “future junior scientists”, David Vargas and Priyanka Jain, who worked as interns under my supervision, and made my laboratory experience more fun at CHTM.

I would also like to thank Linda Bugge and Yekaterina Brandt for their support and kindness. My heartfelt thanks to all my friends in Albuquerque, for making my duration of stay here very enjoyable and memorable. A big thanks to Julia and Patti for their love and efforts that made me feel at a home away from home, whenever I visited them. My college friend, Dhushar, also deserves acknowledgement for always finding the time to talk to me, despite her busy schedule, whenever I missed home. Last, but not the least, I would like to thank my spouse, Mohammad Kabir. His exceptional dedication and commitment to his research and work has set standards for me to follow.

INTEGRATION OF CDSE/ZNS QUANTUM DOTS INTO AS-INDUCED ETCHED NANOVOIDS ON GASB

by

Shayla Nahar Bhuiya

B.S. Electronic and Telecommunication Engineering, North South University, Dhaka, Bangladesh, 2011
M.S. Electrical Engineering, University of New Mexico, 2014

ABSTRACT

Quantum dots, due to their small size, portray unique optical properties that are different compared to those of the bulk material. The most apparent of these properties is the excitation of these dots, resulting in emission of photons, which are visible to the human eye as light. More interestingly, the wavelength of these photon emissions does not solely depend on the type of material from which the quantum dot is made; in addition, it depends on the size of the quantum dots. The dots can also be tuned accordingly to emit into the UV or into the infra-red. The colloidal synthesis of CdSe/ZnS quantum dots is presented, to describe their incorporation into nanovoids formed on GaSb membranes. Nanoscale etch-pit formation on GaSb surfaces happens as a result of arsenic (As_2) based *in situ* etch technique. The effect of *in situ* etch technique leading to the formation of the nanovoids was studied. Atomic force microscopy, scanning electron microscope, and transmission electron microscopy were used to characterize the GaSb surface, to investigate the internal structure of the voids, and to

determine the average size dimensions of the voids, and the void density. Furthermore, experiments and measurements were carried out to check the ability of the quantum dots to fluoresce at the high regrowth temperatures inside the molecular beam epitaxy system. CdSe/ZnS quantum dots were used, considering their high stability over time. The quantum dots were further annealed at different temperatures, and optically characterized to investigate if the core-shell structure changed as a result of the high temperature. Encapsulation of these quantum dots into the highly faceted nanovoids offer potential applications for quantum-confined ensembles.

TABLE OF CONTENTS

LIST OF FIGURES

Chapter 1

Introduction

Semiconductor nanocrystals, also known as quantum dots, have attracted considerable attention as an important new class of materials. A fundamental understanding of the physical and electronic properties of this prototypical material that arises from shrinking dimensions to the nanoscale, is described in the first section of this chapter. Besides providing a rich platform for exploring a new phenomenon, the ease of fabricating quantum dots from the solution-phase, and the ability to chemically engineer them to exhibit a wide range of spectral tunability, has led to the emergence of novel technologies in lighting solutions, sensitive photodetectors, solar energy conversion, biological and biomedical fluorescence imaging, labeling, drug delivery, and photodynamic tumor treatment, and cancer radiation therapies. Some of these current and potential applications are presented towards the end of this chapter.

1.1. Quantum dots: Properties and advantages

Quantum dots were first discovered in the early 1980s by Russian physicist Alexie Ekimov in a glass matrix, and by American chemist Louis E. Brus in colloidal solutions. A quantum dot is a semiconductor nanomaterial which has a structure that restricts the motion of electrons and holes in the conduction and valence bands, respectively, in all three spatial directions. The confinement can be due to one, or a combination of, the

following reasons: (a) electrostatic potentials due to doping, strain, impurities or external electrodes, (b) energy bandgap difference between two or more semiconductor materials (such as in the case of core-shell nanocrystal systems), (c) and/ or the presence of a semiconductor surface (e.g. a semiconductor nanocrystal) (Mukherjee and Das, 2011). Their size typically range from 2 to 20 nm (Talapin et al., 2010).

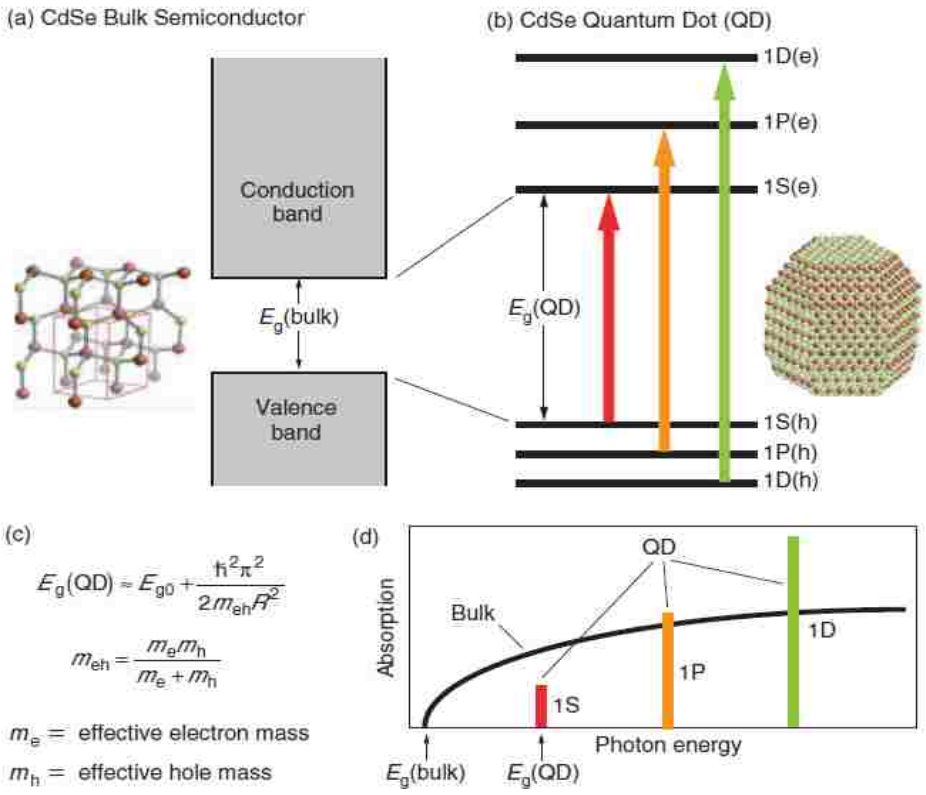

Figure 1.1: Difference in the energy bandgap structure of semiconductors and quantum dots: (a) A bulk semiconductor, such as CdSe, has continuous conduction and valence energy bands separated by a "fixed" energy gap, Eg (bulk). Electrons normally occupy all states up to the edge of the valence band, whereas states in the conduction band are empty. (b) A QD is characterized by discrete atomic-like states with energies that are determined by the QD radius R. These well-separated QD states can be labeled with atomic-like notations, such as 1S, 1P, and 1D. (c) The expression for the size-dependent separation between the lowest electron and hole QD states—Eg (QD), the QD energy gap—was obtained with the spherical "quantum box" model; m_{eh} (d) This schematic diagram represents the continuous absorption spectrum of a bulk semiconductor (black line) compared with a discrete absorption spectrum of a QD (colored bars) (Klimov, 2010).

The electronic properties of quantum dots are between those of bulk semiconductors and discrete molecules. Among the characteristics distinguishing a semiconductor from a quantum dot is the energy bandgap structure between edges of the conduction and valence bands energy, as shown in Figure 1.1. The semiconductor emits light whose frequency, and hence the color, depends on the gap width. When bulk semiconductors of macroscopic sizes are considered, the material's identity determines the energy gap. In this case the gap is a fixed parameter. But nanoscale semiconductor materials of around 10 nm sizes exhibit a different scenario. This range of size is of significance as it refers to the quantum confinement zone. Here, the spatial extent corresponding to the electron wave function becomes comparable to the dot size. As the electrons are confined by the small particle size, their energy levels are 'tuned'. This observed phenomenon is the quantum-size effect, and contributes significantly in QDs. This means that when nanocrystals are made very small so that they approach the Bohr radius, which is the size of an exciton in a bulk semiconductor material, they exhibit quantum confinement. Efros and Efros suggested a simple 'quantum box' [Efros and Efros, 1982] model to describe the quantum-size effect. In this model, the electron movement is restricted in x, y and z directions by impenetrable walls. For a spherical QD with radius R, this model anticipates that a size-dependent factor relating to the energy gap is simply proportional to $1/R^2$. This means that the gap increases as the QD size decreases. Quantum confinement leads to a breakdown of the continuous energy levels of a bulk material into discrete energy levels. This leads to a discrete absorption spectrum of QDs, which contrasts with the continuous spectrum of a bulk semiconductor. Therefore, a quantum dot has a discrete quantized energy spectrum.

The presence of discrete quantum levels gives rise to the interesting and useful properties observed in quantum dots. This indicates that the quantum dots can emit at different wavelengths, as the size of the quantum dot is varied. The smaller the nanocrystal is, the larger the spacing between the energy levels. This larger energy gap leads to a shorter wavelength of fluorescence. For semiconductor nanocrystals, controlling the size of the QDs can, therefore, allow us to control precisely the color at which they emit (Kim et al., 2013). This is one of the most significant advantages of a nanocrystal.

Another major advantage of producing nanoscale crystals is the reduction in crystal defects. We know that the probability of the number of defects in a crystal or lattice is proportional to the size of the crystal. Thus, nanocrystals are less likely to have defects in comparison with bulk crystals. This allows production of high quality fluorescent nano-crystals.

1.2. Inorganic luminescent nanocrystal quantum dots

The nanocrystal quantum dots can be made from organometallic compounds. They are composed of a semiconductor capped with an organic layer. This organic capping helps prevent uncontrolled growth of the nanocrystals and prevents agglomeration of the particles. It also helps the QDs to be chemically manipulated as if they were big-sized molecules and the solubility and reactivity of the nanocrystals is determined by the type of organic molecules used. The capping also terminates any dangling bonds present on the semiconductor surface. Presence of any dangling bonds reduces the efficiency of emission of the QDs through a loss mechanism, where the electrons are trapped at the semiconductor surface before they are able to emit a photon. Synthesis of colloidal

nanocrystals can be done with nearly atomic precision from a nanometer to about 10 nm. Because of the quantum-size effect, this ability to tune the quantum dot size translates into a means of controlling various quantum dot properties, such as emission and absorption wavelengths. For example, the emission of cadmium selenide (CdSe) QDs, as shown in Figure 1.2, can be tuned from blue to deep red by an increase in the dot radius from 2 to 8 nm (Murray et al., 1993).

Figure 1.2: Colloidal quantum dots irradiated with a UV light. Different sized quantum dots emit different color light due to quantum confinement (Bawendi, 2014).

1.3. Applications of quantum dots

The electrical and optical properties possessed by quantum dots have sparked a lot of interest in the electronics as well as the medical industry. These distinctive properties of nano-sized particles are primarily due to the very high surface to volume ratios for the particles and their quantum-size effects. The unique size-tunable emission property, strong light absorbance, bright fluorescence, high quantum yield and broad absorption

spectra have made quantum dots very attractive as biological probes for molecular recognition, fluorescent labeling of biological cells (Cheki et al., 2013), drug delivery (Gao et al., 2004), and therapeutic applications (Yaghini et al., 2009). Other potential applications include bio-analytical assays for diagnosis of diseases, ionizing radiation detection and nanophosphors for solid-state lighting and display.

1.3.1. Biomedical fluorescent labeling and imaging

Among the various applications of quantum dots, biomedical fluorescent imaging has generated the most interest. A quantum dot can be engineered to bind to a specific bio-molecule by modifying the surface ligands. The fluorescence from the dot can then be used to image the location of the molecule in the body, or to investigate its environment. This can be particularly useful in cancer diagnosis, where the quantum dot is tailored to bind to specific DNA sequences associated with the cancer. When the dots are then excited, the cancer-associated DNA sequences would be visible for examination. The ability of the dots to image, and locate multiple molecular targets in parallel, is an extremely powerful biomedical tool, specifically in cancer diagnosis, where early detection depends on identifying a substantial number of genes and proteins.

In contrast to conventional organic dyes and fluorescent proteins, the QDs have broad absorption bands. This means a single light source is sufficient in exciting multiple QDs. This significantly simplifies instrumental design and increases the speed of detection. Furthermore, the QD emission bands are observed to be narrow, (can be as narrow as 20 nm in the visible range). This in principle enables distinct signals to be detected simultaneously with minimal cross talk. Fluorescent proteins, on the other hand, have

narrow absorption bands and relatively wide emission bands, which lead to difficulty in separating signals from distinct fluorophores. Moreover, the colloidal quantum dots are highly stable against photobleaching, unlike organic dyes. This makes them more suitable for monitoring in biological systems for a longer duration (Smith et al., 2006). Yet another advantage of QDs over organic dyes is their ability to fluoresce 10-20 times stronger than organic dyes. This brings forth sensitive detection of analytes in lower concentrations, which are deemed significant for sparsely distributed cancer markers (Bruchez Jr., 1998; Chan, 1998).

In 2003, Wu *et. al*. (Wu et al., 2003), at "Quantum Dot Corporation", Hayward CA, reported the development of quantum dot based biological probes to specifically label the breast cancer marker Her2. Her2 is a cell-surface receptor and the probes were used on fixed and live cancer cells from mouse mammary glands. The authors, also, reported that the two different colored probes could light up distinct cellular components, as they observed with Her2 on the cell surface and proteins in the nucleus. The QD based probes fluoresced more brightly than comparable organic dyes.

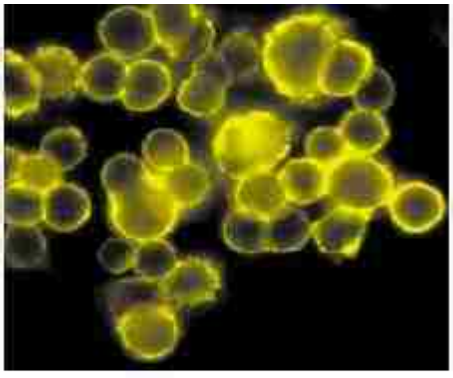

Figure 1.3: Breast cancer cells are labeled with a quantum dot conjugate. The breast cancer marker Her2 was detected on the cells with a combination of the drug Herceptin, biotinylated goat anti-human immunoglobulin G, and quantum dots conjugated to streptavidin (Wu et al., 2003).

1.3.2. Potential application: Nanophosphors for solid-state lighting

White LEDs are produced by combining inorganic phosphors such as cerium-doped yttrium aluminum garnet (YAG: Ce) with blue indium gallium nitride (InGaN) light-emitting diodes (LEDs). However, the blue nitride-based LEDs that excite the yellow-green-emitting YAG: Ce phosphors have an undesired cold, white emission. This emission needs to be made warmer by the addition of red emitting phosphors. Phosphors, generally made from rare-earth elements, tend to emit over a broad spectrum. As such, most of the photons produced by an LED may be rendered by a phosphor into 'wasted' light, which reduces the efficiency of the device altogether. According to past research study (Jia and Hunter, 2006; Neeraj et al., 2004; Xie and Hirosaki, 2007), oxide and sulfur-based phosphors are conventionally used. The oxide-based phosphors incur high levels of thermal quenching at elevated temperatures, while the sulfide-based red phosphors are moisture sensitive as well as suffering from fluorescence saturation, when the forward-bias current is increased and blue emission from the LED becomes intense. Nitride phosphors were also suggested based upon their high photostability as a red phosphor, but failed to create a commercial interest owing to their expensive synthesis methods (Kwak et al., 2012). These drawbacks did not permit a sufficiently high color rendering index (CRI), and therefore made the use of inorganic phosphors limited. The ideal red emitter would be one that has a broad blue absorption and a narrowband emission. The narrowband red emission condition would allow a high luminous efficacy of radiation (LER). LER refers to the lumens of light emitted per Watt, and a high value would result in warm white light with a high CRI and low correlated color temperature (CCT). The red emitters would also need to have a high quantum yield (QY) when

subjected to blue excitation, high photostability, less thermal quenching, low scattering losses and ability to resist fluorescence saturation under high excitation from intense blue emissions from nitride-based LEDs.

Quantum dots, or semiconductor nanocrystals, have been researched as an alternative to satisfy the above criteria (Shea-Rohwer et al., 2012). They behave like phosphors but can be tuned to radiate any color from red to yellow by varying the nanocrystal size, because of the quantum confinement effect previously described in Section 1.1 of this chapter. In 2008, Ziegler et al. (Ziegler et al., 2008) demonstrated an LED made from silica-coated InP/ZnS QDs combined with a green phosphor and YAG with a CRI value of approximately 86 (The ideal white light source has a CRI of 100). Later in 2010, by directing light from an LED through a sheet of quantum dots, the quantum dot LEDs manufactured by QD Vision and Nexxus Lighting offered a narrow spectral emission (~30 nm FWHM) and a more selective optical downshift of the bluer emission from the LED into redder light. These resulted in a CRI of greater than 90%, a superior CCT of 2,700 K and an industry-leading efficacy of 65 lm/Watt (Hogan, 2014). Quantum dots, therefore, are key players in solid-state lighting (SSL) sources owing to their role in maintaining high luminous efficiency, high color quality and consequently, lower power consumption.

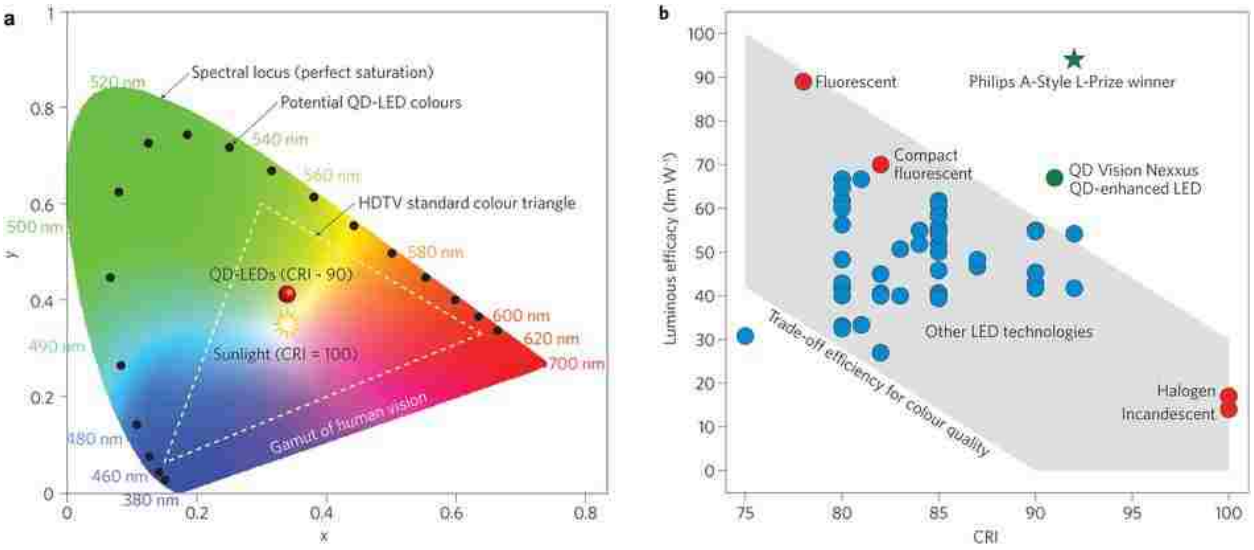

Figure 1.4: Optical advantages of colloidal QDs for display and SSL applications. (a) A CIE chromaticity plot showing that the spectral purity of quantum dots enables a larger range of color than a high definition television (HDTV). (b) Plot of "luminous efficiency Vs CRI" for different commercially produced lighting solutions. Two companies, QD Vision and Nexxus lighting, as shown by the green dot, manufactured the first QD-based SSL source which had a high CRI without trading-off high luminescence efficacy (Shirasaki et al., 2013).

1.4. Objective and scope of thesis

The first chapter of this thesis provides an introduction to quantum dots and their current and potential applications, in an effort to explain the drive for research in this field and its significance in the healthcare and semiconductor optoelectronics industry. The second chapter deals with understanding the concept of the core-shell nanocrystals, the basics of colloidal synthesis, and finally describes the procedure of synthesis of the cadmium selenide/zinc sulphide quantum dots used in this project. A detailed explanation of the in-situ nanoscale etch-pit formation on the surface of the GaSb (100) in the molecular beam epitaxy is covered in the third chapter. The subsequent chapter covers the experiments performed and measurements carried out to achieve the incorporation of the quantum

dots into the nano-scale etch pits, or ‘nanovoids’. Finally, the fifth chapter concludes this work, and provides some insights on potential future work.

References

Bawendi, M.G., 2014. MIT Bawendi Group. URL http://nanocluster.mit.edu/research.php (accessed: 04 May 2014).

Bruchez Jr., M., 1998. Semiconductor Nanocrystals as Fluorescent Biological Labels. Science. 281 (5385), 2013–2016.

Chan, W.C., 1998. Quantum Dot Bioconjugates for Ultrasensitive Nonisotopic Detection. Science. 281 (5385), 2016–2018.

Cheki, M., Moslehi, M., Assadi, M., 2013. Marvelous applications of quantum dots. Eur. Rev. Med. Pharmacol. Sci. 17, 1141–8.

Efros, Al. L., and A. L. Efros. 1982. Pioneering Effort I. Sov. Phys. Semicond. 16, 772

Gao, X., Cui, Y., Levenson, R.M., Chung, L.W.K., Nie, S., 2004. In vivo cancer targeting and imaging with semiconductor quantum dots. Nat. Biotechnol. 22, 969–76.

Hogan, H., 2011. Quantum Dots Warm Up LED Lighting Features. Photonics Spectra,October 2011.URL http://www.photonics.com/Article.aspx?AID=48565 (accessed: 04 May 2014).

Jia, D., Hunter, D.N., 2006. Long persistent light emitting diode. J. Appl. Phys. 100, 113-125.

Kim, J.Y., Voznyy, O., Zhitomirsky, D., Sargent, E.H., 2013. 25th anniversary article: Colloidal quantum dot materials and devices: a quarter-century of advances. Adv. Mater. 25, 4986–5010.

Klimov, V.I., 2010. Nanocrystal Quantum Dots. Boca Raton, FL: CRC Press, 485.

Kwak, S.Y., Ree Kim, N., Kim, J.H., Bae, B.S., 2012. High color rendering white light-emitting diodes based on a green silicate phosphor mixed with a red dye-bridged hybrid. RSC Adv. 2 (32), 12371-12377.

Mukherjee, S., Das, U., 2011. Quantum dots: An optimistic approach to novel therapeutics. Int J Pharm Sci Rev Res 7, 59–64.

Murray, C.B., Norris, D.J., Bawendi, M.G., 1993. Synthesis and characterization of nearly monodisperse CdE (E= sulfur, selenium, tellurium) semiconductor nanocrystallites. Journal of the American Chemical Society 115 (19), 8706–8715.

Neeraj, S., Kijima, N., Cheetham, A.K., 2004. Novel red phosphors for solid-state lighting: the system $NaM(WO_4)_{2-x}(MoO_4)_x$:Eu^{3+} (M=Gd, Y, Bi). Chem. Phys. Lett. 387 (1), 2-6.

Shea-Rohwer, L.E., Martin, J.E., Cai, X., Kelley, D.F., 2012. Red-emitting quantum dots for solid-state lighting. ECS J. Solid State Sci. Technol. 2 (2), R3112–R3118.

Shirasaki, Y., Supran , G.J., Bawendi, M.G.,Bulovic, V., 2013. Emergence of colloidal quantum-dot light-emitting light-emitting technologies. Nat. Photonics 7, 13–20.

Smith, A.M., Dave, S., Nie, S., True, L., 2006. Multicolor quantum dots for molecular diagnostics of cancer. Expert Rev. Mol. Diagn. 6 (2), 231-244.

Talapin, D. V, Lee, J.S., Kovalenko, M. V, Shevchenko, E. V, 2010. Prospects of colloidal nanocrystals for electronic and optoelectronic applications. Chem. Rev. 110, 389–458.

Wu, X., Liu, H., Liu, J., Haley, K.N., Treadway, J. A, Larson, J.P., Ge, N., Peale, F., Bruchez, M.P., 2003. Immunofluorescent labeling of cancer marker Her2 and other cellular targets with semiconductor quantum dots. Nat. Biotechnol. 21, 41-6.

Xie, R.-J., Hirosaki, N., 2007. Silicon-based oxynitride and nitride phosphors for white LEDs—A review. Sci. Technol. Adv. Mater. 8, 588–600.

Yaghini, E., Seifalian, A.M., MacRobert, A.J., 2009. Quantum dots and their potential biomedical applications in photosensitization for photodynamic therapy. Nanomedicine 4 (3), 353–363.

Ziegler, J., Xu, S., Kucur, E., Meister, F., Batentschuk, M., Gindele, F., Nann, T., 2008. Silica-coated InP/ZnS nanocrystals as converter material in white LEDs. Adv. Mater. 20, 4068–4073.

Chapter 2

Synthesis of colloidal cadmium selenide nanocrystals with zinc sulphide shell

2.1. Introduction to core-shell colloidal nanocrystals

Colloidal semiconductor nanocrystals can be thought of as an onion-like structure composed of at least two semiconductor materials. Also, termed as "colloidal quantum dots", they are composed of an inorganic core surrounded by an organic ligand layer. The electron-hole pair is confined in the inorganic core which acts as a "box" and exhibit properties due to the quantum confinement effect. We can think of the nanocrystal core as a spherical portion of the bulk semiconductor lattice. These cores will aggregate to form larger, thermodynamically more stable structures, in the absence of the surface ligands. The surface ligands are, therefore, important in kinetically stabilizing the nanocrystal cores. Additionally, they can also bond to coordinatively unsaturated surface atoms and offer electronic stabilization (Mikulec, 1999). Nonetheless, a major fraction of these organically passivated core nanocrystals can have a large number of surface trap states. The surface has a significant number of dangling bonds and defects. These surface trap states can be a fast non-radiative recombination channel for photon generated charge carriers. This would, ultimately, result in a decrease in the fluorescence quantum yield (QY). A strategy to address the issue of passivating the nanocrystal's surface is to grow a shell around the core, consisting of a second semiconductor, with a higher band gap as

depicted in Figure 2.1. This gives rise to the concept of the core-shell semiconductor nanocrystals. The shell can thus passivate the surface trap states, and improve the fluorescence efficiency. Furthermore, the shell protects the core from photo-oxidation.

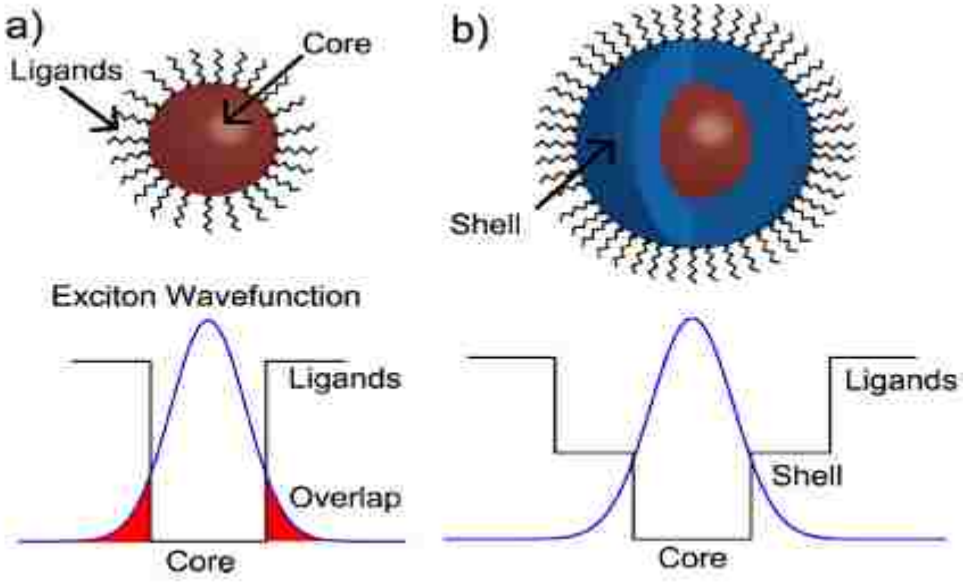

Figure 2.1: (a) Schematic depiction of a quantum-dot core bounded by a coating of ligands, and corresponding electronic structure. Surface ligands solubilize the quantum dot, and aid in partially passivating its surface. Notice the corresponding electronic structure, which shows that an overlap of the exciton still exists between the core and the surface ligands. (b) Growth of an inorganic shell around the quantum-dot core reduces the overlap of the excitons with the surface, to achieve better passivation (Geyer et al., 2013).

Appropriate control of the size, shape and composition of the core and shell materials enable the tuning of the wavelength over a wider range of the spectral window than with either of the semiconductors alone (Reiss et al., 2009).

2.1. Classification of core-shell colloidal nanocrystals

The shell in colloidal semiconductor nanocrystals can have different roles, depending on the energy bandgap and relative position of the electronic energy levels of the semiconductors present. Accordingly, three types can be identified; type 1, reverse type 1, and type 2 energy-level, or band alignment (Reiss et al., 2009).

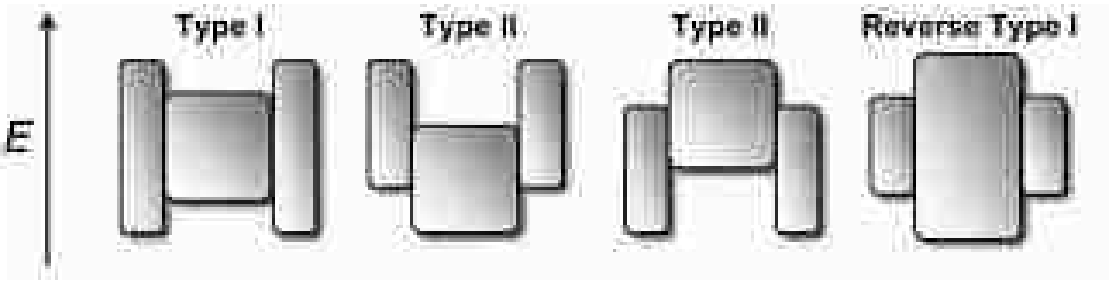

Figure 2.2: Schematic illustration of the energy-level alignment of the three types of core-shell systems realized with semiconductor nanocrystals. The upper edge of the rectangles corresponds to the position of the conduction-band, while the lower edge corresponds to the valence-band of the core-shell semiconductor materials. In each type, the inner rectangles represent the core, while the external rectangles, on either side, represent the shell (Reiss et al., 2009).

Type I: Core-shell nanocrystals of type I have a smaller bandgap for the core compared to the shell. In these types, the conduction and valence band boundaries of the core are found within the bandgap of the shell. This phenomenon confines the electrons and holes in the core. If we assume a cadmium selenide/cadmium sulphide core-shell nanocrystal in Figure 2.2, the electron and hole of an exciton at the CdSe and CdS boundary exhibit energy states within the CdSe core representing the smallest possible energy difference. Compared to an uncoated CdSe quantum dot, the radiation emitted due to electron and hole recombination is red-shifted by a small amount in the core-shell nanocrystal. The

addition of a shell reduces the confinement and thereby decreases the energy state of the excitons, leading to a red-shift in the emission. Examples of such core-shell systems include CdSe/CdS, CdSe/ZnS, and InAs/CdSe (Reiss et al., 2009).

Type II: In this category, the boundaries of the conduction and valence bands of the core are either lower or higher than the corresponding boundaries of the shell. Figure 2.3 shows an example of a type II system containing a ZnTe core (bandgap: 2.26 eV) and CdSe shell (bandgap: 1.74 eV). The smallest separation in energy of the electron and the hole pair occurs when the hole is confined in the ZnTe core valence band and the electron is held in the CdSe shell conduction band.

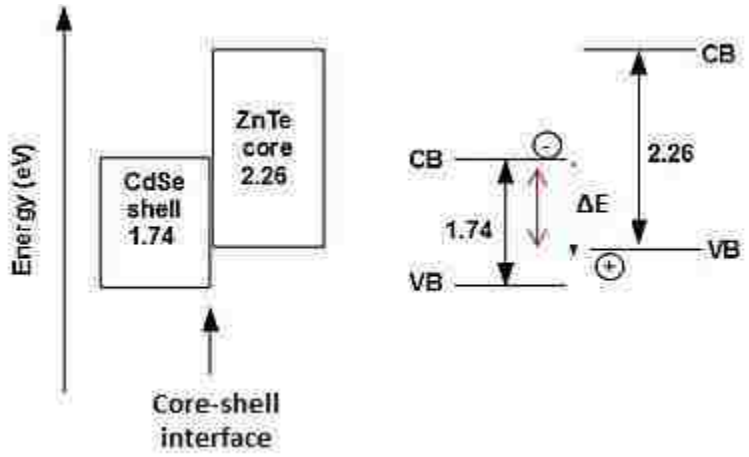

Figure 2.3: A type II core-shell nanocrystal.

The lowest energy difference between the states occupied is shown as ΔE in Figure 2.3. This bandgap will be lower than either of the individual bandgaps (Xie et al., 2005).Therefore, ΔE determines the emission wavelength of the ZnTe/CdSe core-shell nanocrystal. Significant interest in these systems has been generated due to the possibility to vary the thickness of the shell and therefore tune the emission wavelengths towards

regions of the spectrum. These are difficult to achieve with other materials. For example, CdTe/CdSe and CdSe/ZnTe nanocrystals have been synthesized to emit in the near-infrared region (Kim et al., 2003; Reiss et al., 2009).

Reverse Type I: In this configuration the core exhibits a wider bandgap compared to the shell. The shell material has conduction and valence band edges which reside within the edges of the core. As such, the lowest energy separation of an exciton is observed in the case of charge carriers confined in the shell. The emission wavelength can be tuned by changing the shell thickness. Examples of such core-shell systems include CdS/HgS, CdS/CdSe, and ZnSe/CdSe (Reiss et al., 2009).

2.3. Production of semiconductor nanocrystals

High quality semiconductor nanocrystals, or quantum dots, need to be produced without degrading their properties of interest. Section 2.3.1 briefly outlines some of the techniques and knowledge developed in the past years to make these quantum dots, followed by Section 2.3.2, which explains the advantages of the colloidal approach to synthesize quantum dots.

2.3.1. Different approaches to quantum dot synthesis

The production of quantum dots can be broadly classified as either top-down, or bottom-up techniques. The top-down approach involved the use of lithographic techniques, or etching a semiconductor sample down to the required dimensions. In the late 80's, lithography was the main approach used to produce quantum dots, as their dimension

could be predefined. This made them favorable to methodical studies of the quantum confinement effects as a function of the structure (Bayer et al., 1998; Brunner et al., 1992; Ramanathan,S., 2007). Unfortunately this approach led to defects and dislocations that killed the photoluminescence emission of the quantum dots. This lead to the development of other techniques which involved molecular beam epitaxy, metal organic chemical vapor deposition, sol-gel method, high temperature solvent-based wet chemical approach, and arrested precipitation approach at low-temperatures (Murphy et al., 2002). The latter three approaches can be classified under the bottom-up wet synthesis method.

In order to synthesize high-quality monodisperse nanocrystals, such as the II-VI nanocrystals, the high temperature solvent-based approach has been used extensively. This approach has also been successfully used to synthesize III-V semiconductor nanocrystals such as InP and InAs nanocrystals. Generally, in this approach the precursors are added to a coordinating solvent which has a high boiling point. The temperature of the solvent is elevated to a reaction temperature, high enough to allow the precursors to decompose and react, once they are injected into the solvent. The nanocrystals are allowed to form, and then grow before collecting them and dispersing them into a suitable non-solvent. The chemical composition of the reagents, or precursors, and the reaction conditions such as the time, concentration, and temperature can be varied to control the material and size distribution of these colloidal nanocrystals (Ramanathan,S., 2007).

2.3.2 Advantages of colloidal approach in growing quantum dots

Colloidal quantum dot suspensions consist of inorganic dots in an organic or aqueous media. The wet chemical approach to growing colloidal nanocrystals offers several key advantages compared to the other known techniques. First, the chemically controlled approach makes the entire synthesis procedure not only simple to perform, but also cheap and repeatable. This, by itself, is a significant advantage in terms of potential large-scale manufacturing of the nanoparticles. Secondly, the ability to prepare nanocrystal samples displaying uniformity in size, composition, shape and surface chemistry has enabled mapping of their size-dependent material properties. As such, a systematic study of the electronic and optical properties related to these nanoscale materials can be exploited for various applications such as optoelectronic devices, and biological imaging and labelling. Finally, the colloidal nanocrystals can be synthesized separately from their user-end application. Consequently, they can be optimized externally, before incorporating them as internal emitters into photonic crystals, as an example (Richter et al., 2003; Yang et al., 2008) .

The synthesis of II-VI semiconductors, such as CdSe, CdTe, etc., is a high-temperature solvent-based approach which provides a repeatable method to produce uniform quantum dot colloidal samples at the convenience of bench-top conditions (Murray et al., 1993).

2.4. Basics of colloidal synthesis: Nucleation, growth, and Ostwald ripening

Typical synthesis of colloidal quantum dots is based on a three component system which involves precursors, organic surfactants, and solvents. The synthesis occurs in several consecutive stages; nucleation, growth, Ostwald ripening, and isolation of the nanoparticles which reach the desired size from the reaction mixture. The concentration and chemistry of the precursors and surfactants, temperature, growth time and the surfactant-to-precursor ratio are the factors which control these various stages of synthesis. The key to synthesis of monodisperse colloidal quantum dots is the rapid injection of organometallic precursors into a reaction vessel containing a hot coordinating solvent. This elevated temperature decomposes the precursors into monomers. Once the monomers achieve a high enough supersaturation level, the nanocrystal growth begins with a nucleation process. As the nucleation event progresses, the concentration of the monomers or reactant species begins to drop below the required critical concentration for nucleation. Subsequent addition of reagents will result in the growth of the nanocrystals on existing nucleation sites. One of the most critical factors that need to be monitored during the growth process of the nanocrystals is the temperature. It must be high enough to facilitate rearrangement and annealing of atoms during the synthesis progression, and also be low enough to support crystal growth (Murray et al., 2001; Malik et al., 2013; “,” 2007).

Semiconductor nanocrystals often exhibit growth through Ostwald ripening; which is a mechanism where the largest particles in the solution grow at the cost of dissolving smaller ones. The smaller nanocrystals have a higher surface energy, which promotes

their dissolution resulting in the materials redepositing on the larger nanocrystals. Ostwald ripening is a thermodynamically driven spontaneous mechanism seen in solid (or liquid) solutions, which occurs because larger particles are more energetically favored than smaller particles. The molecules residing on the surface of a particle are less energetically stable compared to the other well-arranged ones packed in the interior. Larger particles have a low surface to volume ratio, and as such, have fewer molecules residing on their surface (which is energetically unfavorable) causing the particle overall to be in a lower energy state. As the system, consisting of large and small particles, attempts to lower its overall energy state molecules on the surface of the smaller particle will tend to diffuse through the solution and accumulate on the surface of the larger particles. For a given initial concentration of reagents, a critical size of the nanocrystals exists. If the nanocrystals are smaller than the critical size, they begin dissolving while the larger ones keep growing. As the reaction proceeds, the smaller nanocrystals formed initially disappear, and act as a fuel for the growth of the bigger nanocrystals. The growth rate of the nanocrystals depends on the size of the existing nanocrystals in the system. Peng et al. (Peng et al., 1998) described this growth phenomenon in two regimes, so called "focusing" and "defocusing" of size distribution of the nanocrystals. When the monomer concentration is high, the critical size is relatively small, resulting in the growth of nearly all particles. Smaller crystals grow faster than the larger crystals (as they need more atoms to grow than smaller crystals) during this process. This results in "focusing" of the nanocrystal size distribution, and yields nearly monodisperse particles. When the reagent concentration is depleted during growth, the critical size becomes larger than the average size of the nanocrystals. As a result, the size distribution "defocuses" or

broadens. This is Ostwald ripening where the smaller nanocrystals dissolve at the expense of growing larger ones. Further injection of additional reagents can refocus the size distribution by bringing down the critical size back to a smaller value. Thus, the critical size is dependent on the concentration of reagents. Increasing the temperature can also increase the average nanocrystal size distribution, as it enhances the Ostwald ripening. This increase in size occurs with a compensating decrease in nanocrystal number (Yin and Alivisatos, 2005).

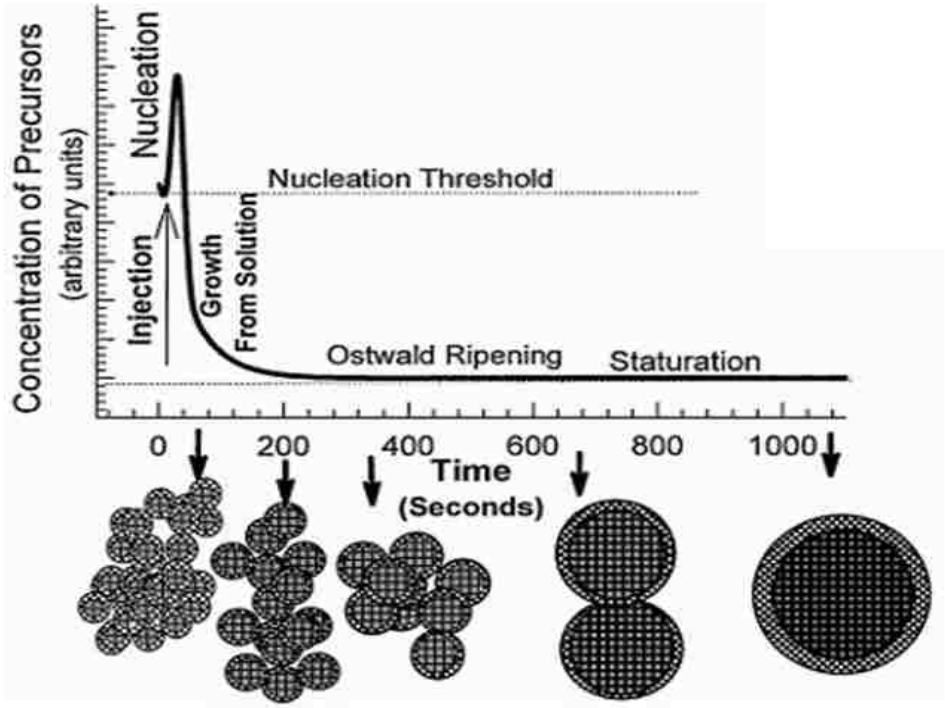

Figure 2.4: 2Cartoon depicting the stages of nucleation and growth for the preparation of monodisperse NCs. As NCs grow with time, a size series of NCs may be isolated by periodically removing aliquots from the reaction vessel (Murray et al., 2000)

The ratio of the concentration of reagents to the surfactants can also play a role in controlling the size of the nanocrystals. As the precursor to surfactant ratio is decreased, smaller nuclei and thus smaller size nanocrystals are produced (Hyeon et al., 2001;

Iwamoto et al., 2009). Furthermore, nanocrystal size was found to be inversely proportional to the surfactant concentration (Choi et al., 2011; Hyeon et al., 2001). The chemistry of the surfactant can, likewise, affect the nanocrystal size. A surfactant which has a higher tendency to bind tightly to the surface of the nanocrystal defined by a higher binding constant of the surfactant groups to the surface, lowers the rate of material addition to nanocrystals being formed in a solution. As a result, average size of nanocrystals produced becomes smaller (Di Ventra et al., 2004). Finally, the size of the nanocrystals can also be increased through the addition of more reagents, whilst controlling the rate of material addition, and temperature.

Once the nanocrystal samples reach the desired size, rapid quenching of the reaction mixture can prevent further growth. In nanocrystal dispersion, interaction amongst the nanocrystals is through the surface, i.e., through the surfactants (ligands). If the interaction between the capping groups and the solvent is strong enough to provide an energetic barrier (or steric repulsive force) to counteract the Van der Waal's forces of attraction between the nanocrystals, then the nanocrystal dispersion is stable. Larger nanoparticles have a larger contact surface, leading to a stronger Van der Waal interaction, and may aggregate first (if the steric hindrance between the capping agents is not strong enough to keep them dispersed evenly) (Ghezelbash, 2006).

Like all chemical reactions, synthesis of nanocrystals is also based on collisions between molecules which occur soon after decomposition of the reagents, and the nucleation event. The growth, size, shape and properties of nanocrystals can be regulated by controlling the reaction temperature, growth time, concentration of the reactant species and surfactants, and the ratio of precursors to surfactants.

2.5. Laboratory set-up for the colloidal synthesis

The synthesis of CdSe/ZnS colloidal quantum dots is performed using the wet chemical "bottom-up" method. This requires a specialized laboratory system known as the Schlenk line. Its purpose is to deliver either vacuum or an inert gas (such as argon), under tightly regulated conditions. Colloidal synthesis needs to be carried out in an inert atmosphere in order to allow handling of air-sensitive precursors and eliminate any possibility of contamination and/or oxidation of the synthesized nanocrystals. The Schlenk line manifold meets these requirements as well as removes any gas by-products throughout the synthesis process.

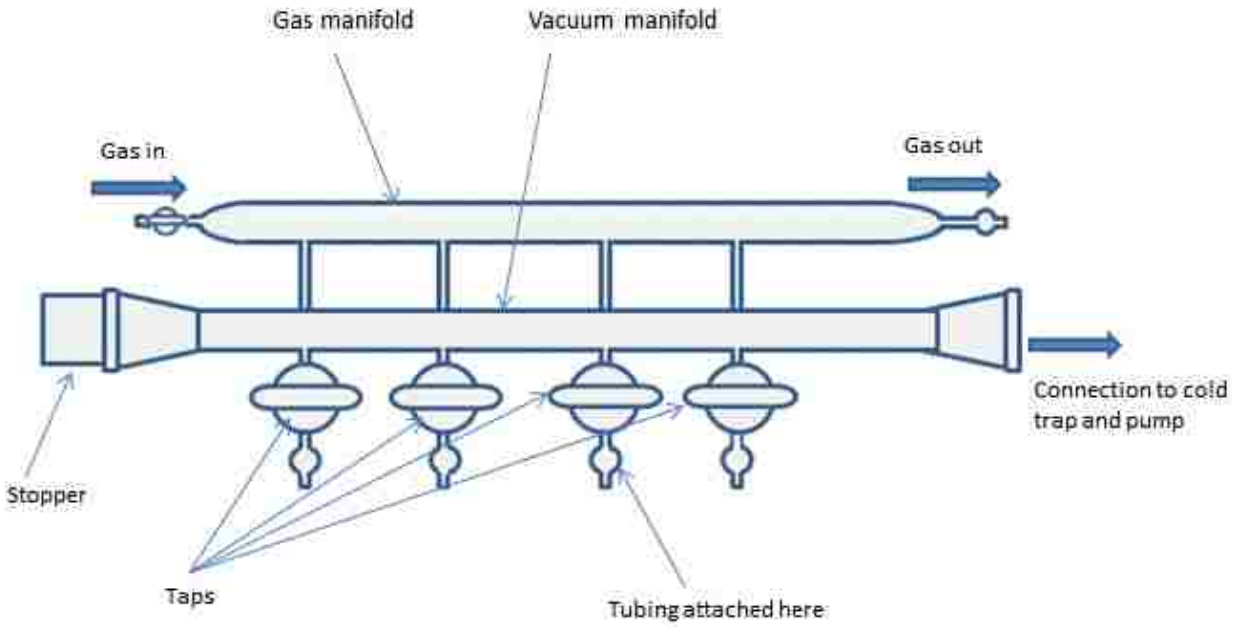

Figure 2.5: Schematic to depict the basic layout of the Schlenk line manifold (Millar, 2012).

The Schlenk line consists of two parallel glass tubes; one connected to the vacuum, and the other connected to an inert gas supply, as shown in Figure 2.5. The two-way valves, or taps, allow switching between the gas and vacuum lines as required throughout the reaction. A Schlenk line usually has around four to six valves to facilitate multiple reactions simultaneously. Flexible rubber or plastic tubing is employed to connect the reaction apparatus to the system. The reaction flask is a three-neck round-bottom flask. The center neck is connected to the Schlenk line rubber hose via a nitrogen adapter. A thin film of silicon grease can be applied to the adapter to make the joint air-tight. The other two necks of the flask are sealed using a rubber septa, and a thermocouple is inserted through one of them into the flask. The thermocouple is connected to a closed-loop p-i-d ramping temperature controller, to vary the reaction temperatures, as required. The round-bottom flask can be heated by placing it firmly on a heating mantle. This ensures good thermal contact. A magnetic stirring controller is placed underneath the heating mantle. This facilitates continuous stirring of the solution in the reaction flask, when a small teflon-coated stir bar is placed inside the flask. Figure 2.6 shows a schematic of the setup described above.

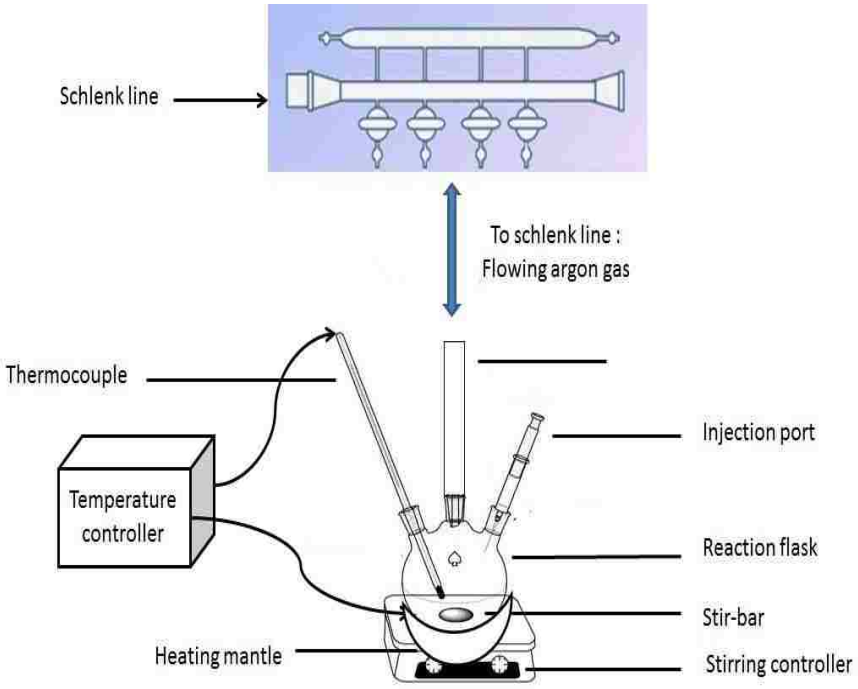

Figure 2.6: Schematic representation of the apparatus set-up for the colloidal synthesis

A glovebox, filled with argon gas, at a pressure of 4-8 bars, is used to handle the air-sensitive chemicals during the synthesis. It has an antechamber port with a sliding tray to transfer chemicals into and out of the box. The water vapor and oxygen level sensors should read levels of 0.1 ppm or less.

All glassware used for the synthesis is pre-cleaned by first treating it with a dilute base and rinsing with water. Next, glass equipment is placed in an acid bath and rinsed with water again. The typical chemical laboratory safety standards are ensured, such as wearing lab coats, googles, face-shields, and appropriate gloves. The colloidal synthesis is carried out strictly in the fumehood chamber, and any chemical waste is disposed according to institutional regulations. Air-quality analyzers, gas detectors, chemical spill-

kits, and first-aid kits are available inside the synthesis laboratory, in the event of an emergency or accident.

2.6. Procedure for synthesis of CdSe colloidal nanocrystals with ZnS coating

The procedure for colloidal synthesis of CdSe/ZnS Direct Shell (DS) was adapted from Clapp et. al. (Clapp et al., 2006). The CdSe core was prepared using cadmium acetylacetonate ($Cd(acac)_2$) and troctyl phosphine selenide. The ZnS direct shell was synthesized using diethylzinc ($ZnEt_2$) and hexamethyldisilathiane (TMS_2S) as precursors.

First 10 mL of trioctyl phosphine (TOP) and 0.79 g of selenium (Se) were mixed to create a 1 M stock solution of TOP:Se in a 250 mL beaker. 20 g of trioctyl phosphine oxide (TOPO), 10 g of hexadecylamine (HDA), and 5 ml of TOP were added to a three-neck flask, which was than degassed in a vacuum and heated to 130 °C for 1.5 hours. Next, the precursor was made by mixing 20 mg of $Cd(acac)_2$, 1.20 g of hexadecanediol (HDDO), and 10 mL of in a three-necked flask and heating it to 100 °C under vacuum, followed by cooling it to 80 °C. After that, 10 mL of the 1 M TOP:Se stock solution was injected into the precursor. After 1.5 hours, the atmosphere was switched to argon and the temperature was raised to 340-350 °C. Under UV light, 30 mL of cadmium and selenium precursors were injected rapidly into the hot solvent flask. The core of the NCs was allowed to grow in this solution for about 3-4 minutes and finished forming as the color changed to green, under the ultraviolet (UV) lamp. As soon as the solution turned green, the temperature was lowered to 130 °C. The hot injection technique of rapidly injecting

the precursors into the hot solvent, followed by a temperature drop, separates the nucleation event from the growth stage and satisfies the requirement for narrow size-distribution of the nanocrystals.

Next, the ZnS coating was synthesized. The temperature of the quantum dot/ TOPO solution was decreased to 140-180 °C. 5 ml of TOP was then added to a beaker. After that, 2.69 ml of 1 M diethylzinc and sulfur precursor (TMS_2S) were added to the TOP in the beaker. Then, 10 mL of the Zn and S precursor solution was very slowly added to the QD/TOPO solution and the temperature was lowered to 80 °C. The solution was stirred for several hours followed by addition of equal amounts of butanol and hexane.

The resultant QDs were harvested by centrifugation using methanol, until a clear supernatant was observed. The supernatant was then discarded leaving the QDs as a precipitate.

Finally, the QDs were collected using hexane, and stored in a glass vial, as shown in Figure 2.7.

Figure 2.7: Synthesized CdSe/ZnS DS QDs emitting around 570 nm (greenish-yellow), under the UV lamp.

References

Bayer, M., Walck, S., Reinecke, T., Forchel, A., 1998. Exciton binding energies and diamagnetic shifts in semiconductor quantum wires and quantum dots. Phys. Rev. B 57, 6584–6591.

Brunner, K., Bockelmann, U., Abstreiter, G., Walther, M., Böhm, G., Tränkle, G., Weimann, G., 1992. Photoluminescence from a single GaAs/AlGaAs quantum dot. Physical review letters 69 (22), 3216–3220.

Choi, D.H., Jeong, G.H., Kim, S.W., 2011. Fabrication of size and shape controlled cadmium oxide nanocrystals. Bull. Korean Chem. Soc. 32, 3851–3852.

Clapp, A.R., Goldman, E.R., Mattoussi, H., 2006. Capping of CdSe-ZnS quantum dots with DHLA and subsequent conjugation with proteins. Nat. Protoc. 1, 1258–66.

Geyer, S.M., Scherer, J.M., Jaworski, F.B., Bawendi, M.G., 2013. Multispectral imaging via luminescent down-shifting with colloidal quantum dots. Opt. Mater. Express 3, 1167.

Ghezelbash,H.A., 2006. Topics in Colloidal Nanocrystals Synthesis and characterization. Dissertation-The University of Texas at Austin, 16-17.

Murray, C. B., Sun, S., Gaschler, W., Doyle, H., Betley, T. A., MKagan, C. R. (2001). Colloidal synthesis of nanocrystals and nanocrystal superlattices. IBM Journal of Research and Development, 45 (1), 47-56.

Hyeon, T., Lee, S.S., Park, J., Chung, Y., Na, H.B., 2001. Synthesis of highly crystalline and monodisperse maghemite nanocrystallites without a size-selection process. J. Am. Chem. Soc. 123, 12798–801.

Iwamoto, W., Holanda Jr., L.M., Vargas, J.M. , Pagliuso, P.G., Rettori, C., Oseroff, S.B. (2009). Synthesis and characterization of Gd3+ ions doped in $NaYF_4$ nanocrystals. 3rd International Conference on Integrity, Reliability and Failure, Portugal, 20-24 July 2009, 7-9.

Kim, S., Fisher, B., Eisler, H.J., Bawendi, M., 2003. Type-II quantum dots: CdTe/CdSe(core/shell) and CdSe/ZnTe(core/shell) heterostructures. J. Am. Chem. Soc. 125, 11466–7. doi:10.1021/ja0361749.

Malik, P., Gulati, N., Malik, R.K., Nagaich, U., 2013. Carbon nanotubes , quantum dots and dendrimers as potential nanodevices for nanotechnology drug delivery systems. International Journal of Pharmaceutical Sciences and Nanotechnology 6 (3), 2113–2124.

Mikulec, F.V., 1999. Semiconductor nanocrystal colloids: manganese doped cadmium selenide, (core)shell composites for biological labeling, and highly fluorescent cadmium telluride. Doctoral dissertation, Massachussetts Institute of Technology.

Millar, S., 2012. Air-sensitive techniques (1). URL http://www.chemistryviews.org/details/education/3728881/Tips_and_Tricks_for_the_Lab_Air-Sensitive_Techniques_1.html (accessed: 04 May 2014).

Murray, C.B., Norris, D.J., Bawendi, M.G., 1993. Synthesis and characterization of nearly monodisperse CdE (E= sulfur, selenium, tellurium) semiconductor nanocrystallites. Journal of the American Chemical Society 115 (19), 8706–8715.

Murphy, C. J., Coffer, J. L., 2002. Quantum dots: A primer. App. Spectrosc. 56 (1), 16A-27A.

Peng, X., Wickham, J., Alivisatos, A.P., 1998. Kinetics of II-VI and III-V colloidal semiconductor nanocrystal growth: " focusing " of size distributions 7863, 5343–5344.

Ramanathan,S., 2007. Polarization studies of coupled quantum dots. Thesis, Ohio University.

Reiss, P., Protière, M., Li, L., 2009. Core/shell semiconductor nanocrystals. Small 5 (2), 154–68.

Richter, S., Schweizer, S., Jamois, C., Steinhart, M., Wehrspohn, R.B., Zacharias, M., 2003. Colloidal HgTe Quantum dot emitters in 2D photonic crystal. Annual Report. Max-Planck-Institut für Mikrostrukturphysik: Germany, 34–35.

Xie, R., Zhong, X., Basché, T., 2005. Synthesis, characterization, and spectroscopy of type-II core/shell semiconductor nanocrystals with ZnTe cores. Adv. Mater. 17, 2741–2745.

Yin, Y., Alivisatos, P., 2005. Colloidal nanocrystal synthesis and the organic-inorganic interface. Nature 437, 664–70. doi:10.1038/nature04165

Yang, J., Heo, J., Zhu, T., Xu, J., Topolancik, J., Vollmer, F., Ilic, R., Bhattacharya, P., 2008. Enhanced photoluminescence from embedded PbSe colloidal quantum dots in silicon-based random photonic crystal microcavities. Appl. Phys. Lett. 92, 261110.

Chapter 3

Formation and characterization of nanovoids

Nanopits can be etched onto GaSb substrate using As_2 as the etchant. The etching is done *in situ*, within an MBE system. This process has been extremely successful, as previously demonstrated by Huang *et al.* (Huang et al., 2007). A detailed study of the experimental conditions to establish the As_2 and GaSb reactions and the results of the etched-pit or nanovoid formations is required to better understand their crystallography and exploit them for use in quantum-confined ensembles. Section 3.1 briefly explains the chemical reactions leading to the formation of the nanovoids, while Section 3.2 and 3.3 presents the experimental details, analysis, and characterization of these nanoscaled pits.

3.1. Growth process of the nanovoids

Formation of the nanovoids occurs through an *in situ* etch inside an MBE system, as already mentioned. The etch technique inside the MBE have a significant advantage over regrowth processes, as they ensure that the surface stays free of contaminants or any native oxides. As_2 is a common source in most III-V machines. This process, therefore, aids GaSb etching without making any complex equipment modifications. Following the arsenic-induced etch, GaAs overgrowth continues by coalescence over the etched pits, forming nanovoids at the GaAs/GaSb interface. This is, then, followed by planar growth of the GaAs material. The nanovoids formed have been comprehensively investigated, as described in Section 3.3, and have been found to be highly faceted. This feature of the

nanovoids may allow encapsulation schemes, for the development of novel quantum-confined ensembles (Baier, Watanabe, Pelucchi, & Kapon, 2004). The nano-scale dimensions of the voids would exhibit quantum size effects for the encapsulated material.

GaSb reacts with As_2 due to a negative enthalpy of reaction, as described by Losurdo et al (Losurdo et al., 2006). The As_2 specie reacts strongly with GaSb for both 1) the anion exchange reaction and 2) the isoelectronic AsSb compound formation reaction, where

$$2GaSb+As_2 \rightarrow 2GaAs+Sb_2, \quad \Delta H = -47.6 \text{ kJ/mol, and} \qquad (1)$$

$$GaSb+As_2 \rightarrow GaAs+AsSb, \quad \Delta H = -33.9 \text{ kJ/mol.} \qquad (2)$$

In both reactions, As_2 aggressively reacts with GaSb to form GaAs and either excess Sb (1) or AsSb (2). The etching of GaSb surfaces by As_2, leading to the formation of faceted pits, can be attributed to the above chemical reactions. (Berger & Fekete, 1985; Brewer, McClure, & Osgood, 1985; Ibbotson, Flamm, & Donnelly, 1983). Atomic force microscopy, and transmission electron microscopy has established that further growth inside the MBE, results in the formation of a capping layer of GaAs material over the interfacial pits, to form the nanovoids (Huang et al., 2007).

3.2. Experimental details of the nanovoid formation

The nanovoid samples for this study were grown in a VG V80H MBE system, equipped with a valved As and Sb cracker. The cracking zones were operated at 900 °C, resulting in As_2 and Sb_2 species. The temperature of the substrate was determined using an optical pyrometer, and the substrate's growth surface was monitored *in situ,* by a reflection high energy electron diffraction (RHEED) system. The native oxide on the GaSb substrate was

thermally removed at 540 °C. The growth was initiated with a GaAs smoothing layer at a temperature of 510 °C. A III: V beam equivalent pressure (BEP) ratio of 1:6 was used to grow GaSb. After the RHEED pattern showed a (3x1) reconstruction, which indicates a high quality GaSb surface, the growth was paused by turning off the Ga flux, subsequently the Sb flux was also turned off. The latter allows the excess Sb to desorb from the surface of the GaSb. At this point, As2 flux was introduced on the surface. Under As_2 overpressure for 60 sec, with an approximate beam equivalent pressure (BEP) of 1 X 10^{-6} mbar, and the substrate temperature at 510 °C, the remnants of the (3 x 1) pattern disappear, indicating the GaSb epilayer was etched. The GaAs growth was then initiated. The growth temperature was kept constant at 510 °C. This resulted in a smoothing of the surface, with continued growth for about 20 nm. A III: V BEP ratio of 1:10 was used for the GaAs growth (Huang et al., 2007).

3.3. Characterization of the nanovoids

The As_2-induced etched pits on the GaSb surface were analyzed using a Hitachi S-5200 SEM, as shown in Figure 3.1. (a) and (b). The pits varied in both size and shape. The average dimensions were ~25 nm in width, 50–80 nm in length, and 10–70 nm in depth. The image in Figure 3.1.(b) shows a side-view of (110) cleaved facet to reveal a 30 nm wide pit.

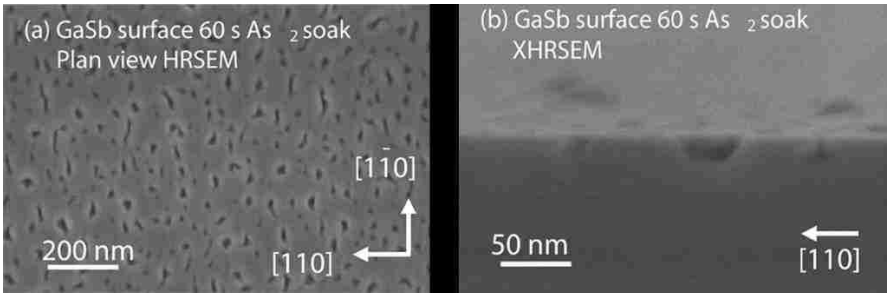

Figure 3.1: (a) Plan view and (b) side view of HRSEM images of etch pits on the GaSb surface after soaking in As_2 for 1 min (Huang et al., 2007)

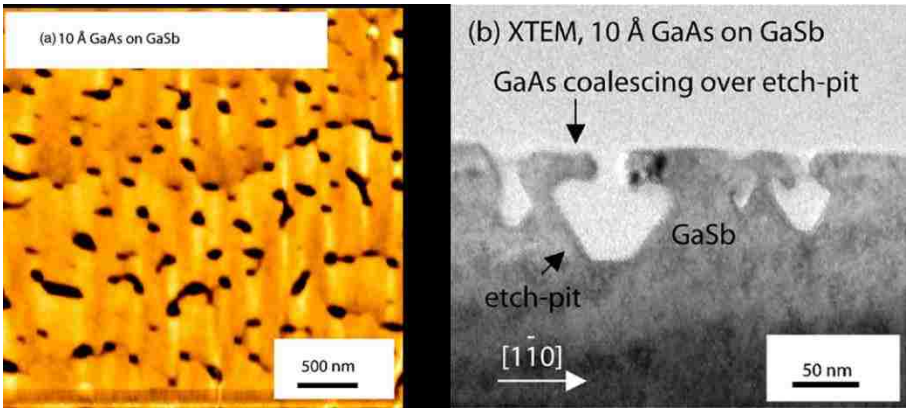

Figure 3.2: The GaAs coalesces partially over etched pits, which are shown by the (a) AFM and (b) XTEM image (Huang et al., 2007).

The resolution available using the HR-SEM was not high enough to understand the faceting of the pits. By grinding samples using mechanical methods to less than 10 µm of thickness and thinning the samples to electron transparency using an ion beam, high resolution cross-section TEM (XTEM) specimens for imaging were prepared. While the HRSEM images in Figure 3.1 show etch pits on the GaSb surface after the As2 influx for 60 sec, the AFM and XTEM images in Figure 3.2. (a) and (b) show the remnants of the existence of the faceted voids on the GaSb surface after about three monolayers (3 MLs) of GaAs were grown. Along with the images in Figure 3.3., they further reveal the progression of the GaAs overgrowth on the etched GaSb surface, with the GaAs coverage

increasing from 3 to 30 monolayers (MLs). The SEM image in Figure 3.1.(a), taken before the growth of the GaAs was initiated, and the AFM image in Figure 3.2.(a), taken after the growth of the GaAs, belong to the same sample and show a consistent pit density of $1x10^9$ /cm^2. If the GaAs deposition is continued, the lateral overgrowth proceeds to coalesce over the pits, resulting in encapsulated nanovoids at the interface. It is further observed, in the TEM images, that no GaAs growth takes place inside the etched pits (Huang et al., 2007).

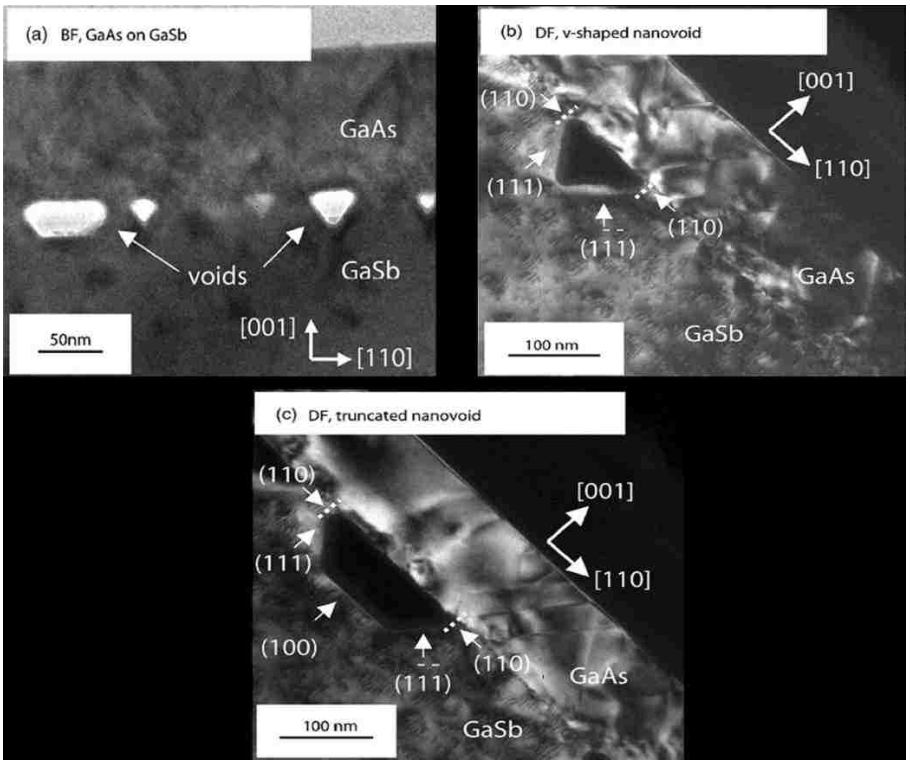

Figure 3.3: XTEM images of GaAs/GaSb interface. Part (a) shows a bright field image featuring nanovoids, while (b) shows a dark field image highlighting a single v-shaped nanovoid. (c) shows a single truncated v-shaped nanovoid (Huang et al., 2007).

Continuation of the growth of GaAs leads to a complete coalescence over the nano-pits. The images in Figure 3.3 show a capping layer of GaAs grown over the nanopits about

100 nm thick. Figure 3.3.(a), specifically, shows a bright field (BF) TEM analysis of v-shaped and truncated v-shaped nanovoids present on the GaAs/GaSb interface. The v-shaped nanovoid is enclosed by (111) and $(1\bar{1}\bar{1})$ sidewalls, while the truncated v-shaped nanovoid is also enclosed by (111) and $(1\bar{1}\bar{1})$ sidewalls but is bounded at the bottom by a (100) plane. The difference in etch rates of the GaAs/GaSb surface along a certain crystallographic direction determines the formation of these facets. In case of such low-index crystal planes, the directional etching rate progressions has been shown to be in the order of (111) > (100) > (110), in a number of III-V material studies(Brewer et al., 1985; Ibbotson et al., 1983).

The dark field (DF) TEM images of the GaAs/GaSb surface shown in Figure 3.3.(b) and (c) highlight the coalescing of the GaAs over the nanovoids. There is a large lattice mismatch between the GaAs and GaSb layer. As a result, strain exists between these two layers. This strain is relaxed through defects, better known as threading dislocations, as can be seen in Figure 3.3(b). The threading dislocation density is significant at the GaAs/GaSb interface as well as, in the GaAs capping layer over the voids. Figure 3.3(c) shows the DF image of a truncated nanovoid, and also elucidates the coalescence of the GaAs over it. This truncated nanovoid is larger than the v-shaped nanovoid, and the capping layer over it seems to have a lower threading dislocation density. This is speculated to be because of the fact that the truncated nanovoids have a larger area of GaAs not in contact with the GaSb, and therefore, they can relieve the strain occurring due to the mismatch more effectively, to result in a lower defect density.

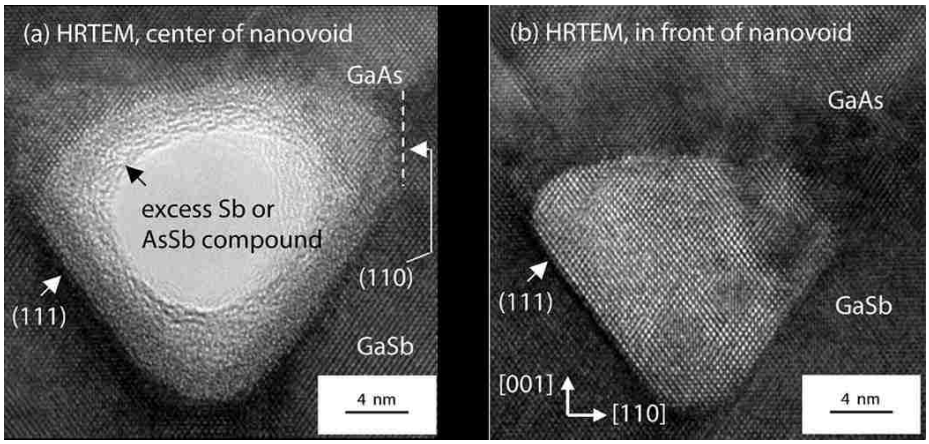

Figure 3.4: HR-XTEM images of (a) a single nanovoid with amorphous surface coating and (b) nanovoid viewed through several layers showing crystalline structure (Huang et al., 2007).

The surrounding material of two different nanovoids is shown in the high resolution TEM images of Figure 3.4.(a) and (b). The thick coating on the {111} planes indicates the presence of amorphous material on the inside of the void. No TEM diffraction pattern is produced by the amorphous material. This amorphous material could either be excess Sb, caused by the anion exchange reaction shown in Equation (1), or it could be the isoelectronic AsSb compound caused by the alternate reaction shown in Equation (2).

The etching rate in (111) planes is thought to decrease because of the amorphous elemental Sb or AsSb layer(Lin, C. L. ; Su, Y. K.; Se, 1998). The accumulation of the surface AsSb or Sb layer occurs to a certain extent, which implies that the rate of etching in the [110] direction occurs at a higher rate than along the [100] direction. This causes the pit to increase in width faster, compared to the rate of increase in depth. The result is a (100) plane in the lowest level along with the formation of truncated v-shaped pits. Crystallographic adatom incorporation above the {111} planes seems to be prevented by this amorphous deposition. Eventually, the overgrowth of GaAs proceeds from the (110)

planes and a coalescing occurs over the pit. Although the overgrowth of the GaAs has been shown in Figure 3.2.(b), the (110) nucleation site can only be seen in the higher–resolution image shown in Figure 3.4.(a)(Huang et al., 2007) .

Figure 3.4.(b) is an XTEM image elucidating the nanovoid as seen through several atomic layers in front of the void. This image allows for only the crystalline material in front of the nanovoid to be seen, since the amorphous material is hidden from view. It can now clearly be seen that the {111} planes are the terminating facets and the {110} planes are the planes on which the nucleation occurs. The difference in material thickness makes the nanovoids appear lighter in contrast to the surrounding material (Huang et al., 2007).

3.4. Etching of the GaAs capping layer to expose nanovoids

A coalescing layer of GaAs grows over the nanopits inherently without any changes in the growth temperature inside the MBE, as previously explained. Since the goal was to incorporate the CdSe/ZnS quantum dots into nanovoids, the GaAs capping layer had to be removed. A $NH_4OH:H_2O_2$ etchant solution, at a volume ratio of 1:33 (Yeh & Smith, 1994) was used to remove GaAs capping layer from GaSb surface. This etchant solution allows selective etching at an etch rate of 5-6 μm/min at room temperature. The solution must be continuously stirred, or placed in an ultrasonic agitator to allow a uniform etch. Although, 100 nm of GaAs capping layer could be etched in less than 1 min, several samples were etched for different times to account for reaction delay (in correspondence with lab-mate, “Emma Renteria”).

A SEM study was conducted to determine if the voids were exposed after the $NH_4OH:H_2O_2$ etch. Figure 3.5 shows top view SEM images of the samples, before being etched with $NH_4OH:H_2O_2$. Figure 3.6 shows SEM images, after the sample was exposed to 1 minute etch. Figure 3.7 shows SEM images after the sample was etched for 5 minutes. These SEM images clearly showed the exposure of the nanovoids. Hence, the nanovoids were ready for the next step in the project, which involved the incorporation of the colloidal quantum dots.

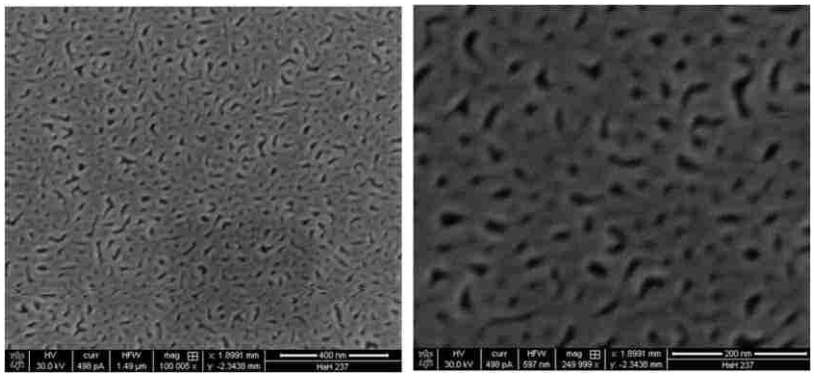

Figure 3.5: SEM top view images of the GaSb nanovoid sample before being etched with $NH_4OH:H_2O_2$.

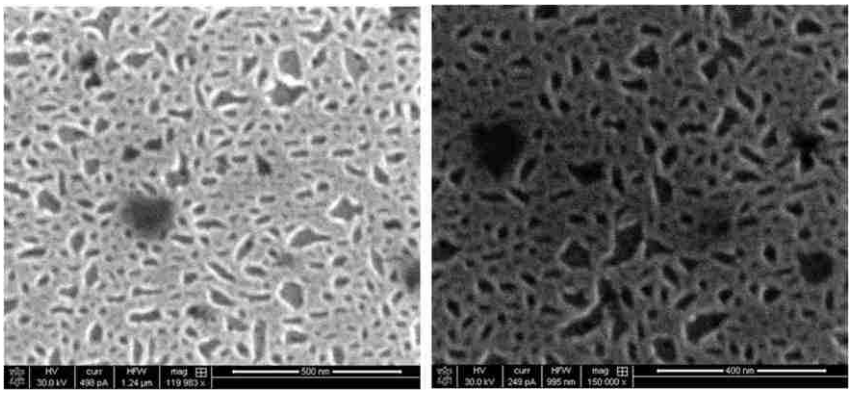

Figure 3.6: SEM images of the GaSb nanovoid sample after been etched with $NH_4OH:H_2O_2$ for 1 min.

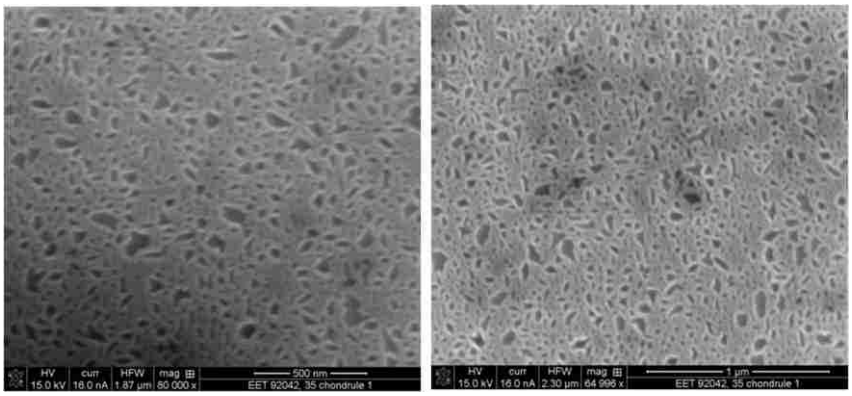

Figure 3.7: SEM images of the sample R12-128 after been etched with $NH_4OH:H_2O_2$ for 5 minutes.

References

Baier, M. H., Watanabe, S., Pelucchi, E., & Kapon, E., 2004. High uniformity of site-controlled pyramidal quantum dots grown on prepatterned substrates. *Applied Physics Letters*, *84*(11), 1943. doi:10.1063/1.1682677

Berger, J., & Fekete, D., 1985. Monolithic integration of AlGaAs/GaAs laser and external mirrors. *Applied Physics Letters*, *46*(9), 806. doi:10.1063/1.95890

Brewer, P. D., McClure, D., & Osgood, R. M., 1985. Dry, laser-assisted rapid HBr etching of GaAs. *Applied Physics Letters*, *47*(3), 310. doi:10.1063/1.96202

Di Ventra, M., Evoy, S., & Heflin, J. R. (Eds.)., 2004. Introduction to nanoscale science and technology. *Springer*, 6, 191.

Huang, S. H., Balakrishnan, G., Mehta, M., Dawson, L. R., Huffaker, D. L., & Li, P. , 2007. Arsenic-induced etched nanovoids on GaSb (100). *Journal of Applied Physics*, *102*(4), 044312. doi:10.1063/1.2772532

Ibbotson, D. E., Flamm, D. L., & Donnelly, V. M., 1983. Crystallographic etching of GaAs with bromine and chlorine plasmas. *Journal of Applied Physics*, *54*(10), 5974. doi:10.1063/1.331775

Lin, C. L. ; Su, Y. K.; Se, T. H. ; L. W. L., 1998. Variety Transformation of Compound at GaSb Surface under Sulfur Passivation Variety Transformation of Compound at

GaSb Surface under Sulfur Passivation. *Japanese Journal of Applied Physics*, *37*(Part 2), L 1543 – L 1545.

Losurdo, M., Capezzuto, P., Bruno, G., Brown, A. S., Brown, T., & May, G., 2006. Fundamental reactions controlling anion exchange during mixed anion heterojunction formation: Chemistry of As-for-Sb and Sb-for-As exchange reactions. *Journal of Applied Physics*, *100*(1), 013531. doi:10.1063/1.2216049

Yeh, H.-J. J., & Smith, J. S., 1994. Integration of GaAs vertical-cavity surface emitting laser on Si by substrate removal. *Applied Physics Letters*, *64*(12), 1466. doi:10.1063/1.111887

Chapter 4

Experiments and Results

Before placing the quantum dots in the nanovoids, we carried out some experiments to determine if the QDs would still have photoluminescence (PL), after being exposed to the high regrowth temperatures inside the MBE system. In order to investigate this, we used silicon wafers as the substrate, to contain the QDs. Steps involved were:

- identification of the type of silicon wafers
- identification of the right etchant
- determination of the etch process and time
- using the Alpha-Step to carry out an etch profile analysis
- calcination (to heat a substance to a high temperature but below the melting or fusing point, causing loss of moisture, reduction or oxidation, and the decomposition of carbonates and other compounds) of the QDs at the regrowth temperature of around 500 °C
- subjecting the wafer containing the QDs to regrowth temperatures, in a vacuum environment
- measuring the photoluminescence emission (PL) and photoluminescence excitation (PLE) spectra of the QDs prior to, and after placing the dots on the etched Si-wafer

4.1. Identification of type of silicon wafer used

Silicon wafers are thin slices of highly pure, and nearly defect-free semiconductor material. They are used as the substrates for the fabrication of integrated circuits and other microelectronic devices. The fabrication procedure involves several steps such as doping, etching, material deposition, and photolithographic patterning. Wafers are sliced according to specific crystal orientations from silicon ingots, which are grown from silicon seed crystals, which have a regular diamond cubic crystal structure. Miller indices, for example, <100> or <111>, are used to define the crystal orientations. The following paragraph is a detailed discussion on how to distinguish silicon wafer <100> from <111>.

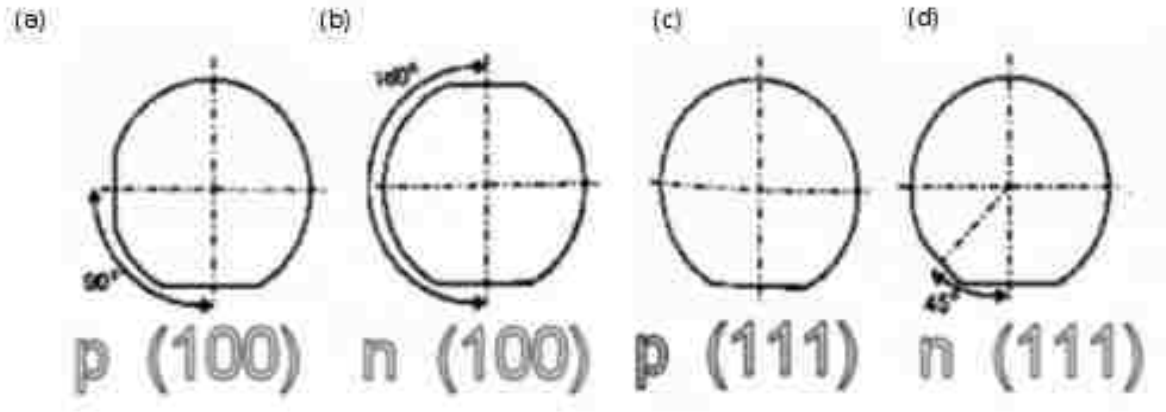

Figure 4.1: By observing the angle between primary and secondary flats we can distinguish silicon wafer <100> from <111>. (a) 90° angle between flats indicates it is a p type <100> silicon wafer (b) 180° angle between flats indicates it is a n type <100> silicon wafer (c) Absence of secondary flat indicates it is a p type <111> silicon wafer (d) 45° angle between flats indicates it is a n type <111> silicon wafer (Islam, 2010).

By observing wafer flats, as shown in Figure 4.1 (a) through (d) we can distinguish between silicon wafer <100> and <111>. The purpose and function of wafer flats is the

orientation for automatic equipment and to indicate type and orientation of crystal (Islam, 2010). There are two flats:

1. **Primary Flat:** The flat of longest length located in the circumference of the wafer. The primary flat has a specific crystal orientation relative to the wafer surface.

2. **Secondary Flat:** The flat of shortest length located in the circumference of the wafer. This flat indicates the crystal orientation and doping of the wafer. The location of this flat varies**.**

We have used p-type <100> silicon wafers for our experiments.

4.2. Etching of the silicon wafer

4.2.1. Anisotropic silicon etch using potassium hydroxide (KOH) solution

KOH is an etchant which attacks silicon preferentially in the <100> plane, producing a characteristic anisotropic V-etch with sidewalls that form a 54.7 ° angle with the surface (35.3 ° from the normal). This etch process is independent of the doping concentration for As, P, and Sb dopants.

- Preparation of the etchant: In order to prepare the 30% etchant, we used 70 g KOH pellets and 190 ml of de-ionized (DI) water. We mixed the pellets on a warm surface of about 80 °C, until the KOH completely dissolved. A stir-bar was placed into the beaker to ensure the mixing was done evenly (UCI , 2014).

KOH is an etchant which attacks silicon preferentially in the <100> plane, producing a characteristic anisotropic V-etch with sidewalls that form a 54.7° angle with the surface (35.3° from the normal). This etch process is independent of the doping concentration for As, P, and Sb dopants.

- Procedure for cleaning the wafer: First, we cleaned the wafer (UIUC Biosensing Inst., 2014) using acetone, isopropyl alcohol (IPA), and DI water. The silicon wafer was placed in a beaker, which was partially filled with acetone. Next, the beaker was placed in an ultrasonic bath (no heat) and the wafer was continued to be agitated (vibrated) for a few minutes. Tweezers were used to remove the wafer from the beaker. The cleaning steps were then repeated with IPA and DI water consecutively. While IPA and acetone helped to remove any organic contaminants from the wafer surface, DI water helped to wash off any ionic contaminants. Finally, the waste cleaning agents were disposed into the appropriate waste container.

The cleaned wafer was placed in a Petri-dish and heated to 80 °C in the oven. About 10 ml of the solution was taken in a pipette, and a drop was placed on the hot wafer. The KOH solution bubbled at the exposed silicon sites, while etching occurred. The etch rate for 30% KOH was 1.3 µm/min, according to Seidel et al. (Seidel et al., 1990), as shown in the table in Figure 4.2. Therefore, we let the wafer etch for one minute, after which it was allowed to cool down. Finally, we cleaned the wafer once again, according to the cleaning procedure mentioned above.

Etchant	Temperature (°C)	Direction (plane)	Etch rate (μm min^{-1})	Remarks	Reference
20% KOH: 80% H_2O	20 40 60 80 100	(100) (100) (100) (100) (100)	0.025 0.188 0.45 1.4 4.1	Near Peak etch rate at the conc. across temperature	[3]
30% KOH: 70% H_2O	20 40 60 80 100 20 40 60 80 100	(100) (100) (100) (100) (100) (110) (110) (110) (110) (110)	0.024 0.108 0.41 1.3 3.8 0.035 0.16 0.62 2.0 5.8	Smoother surfaces than at lower concentration Faster etch rate for (110) than for (100)	[3]

Figure 4.2: The table relates silicon etch rates of KOH as a function of percent composition, temperature, and orientation. As with all wet-chemical etching solutions, the dissolution rate is a strong function of temperature. Adapted from Seidel *et al.* (Seidel et al., 1990).

4.2.2. Etch-profile analysis of the silicon wafer

An etch profile analysis of the wafer was carried out using an Alpha-Step. The one-minute etch done using 30% KOH solution resulted in a depth of 10,000 Å. This is 1.0 micron. This showed that we were able to carry out the etching successfully.

4.3. Calcination of the quantum dots

Now that we created a depression in the silicon wafer, we placed the CdSe/ZnS QDs into it using a pipette. Calcination was then carried out to check if the QDs could withstand the high regrowth temperatures of around 500-600 °C inside the MBE growth chamber. The wafer containing the QDs was placed inside the oven, and heated to 600 °C for fifteen minutes.

PL measurements on the QDs were done both before and after the heat treatment. As shown in Figure 4.3, the QDs exhibited bright fluorescence prior to the calcination process. After calcination, no PL was observed. It is speculated that the organic coating around the quantum dots protected them from oxidation, and, upon calcination, the organic ligands were burned off, leaving behind bare quantum dots that were very susceptible to oxidation, a process that had detrimental effects on the PL of the sample.

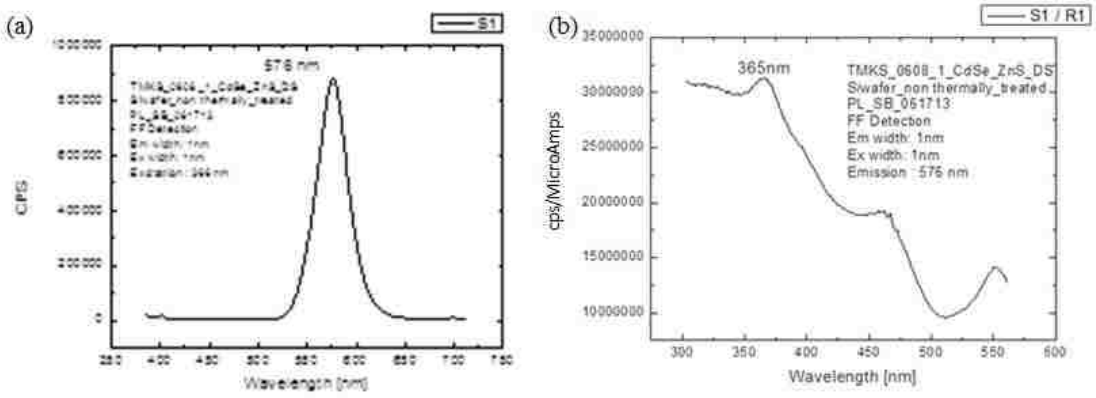

Figure 4.3: Measurements prior to the calcination process (a) PL spectra of the CdSe/ZnS DS QDs (b) PLE spectra of the CdSe/ZnS DS QDs.

4.4. Heat treatment of the QDs in a vacuum environment close to the maximum growth temperature

The intention of heat treatment inside the MBE machine was to simulate the oxygen-free environment, which the QDs would be subjected to, when the capping layer of GaAs was regrown over the exposed nanovoids containing the dots.

At first, a bare clean silicon wafer, without the quantum dots, was placed inside the heating chamber of the MBE, to check for any outgassing. The highest possible temperature that could be reached in this particular chamber was 480 °C (relatively close to the regrowth temperature). This particular chamber could be sealed off from the other growth chambers inside the MBE, thereby, posing no danger of contaminating the other chambers if any outgassing occurred, by monitoring the pressure in the chamber. It was confirmed that the wafer did not outgas more than epi-ready wafers, at the mentioned temperature. This indicated that if any outgassing occurred later, in the subsequent steps, it would be due to the addition of any new substance to the wafer. Next, the CdSe/ZnS quantum dots were pipetted into the depression created on the same silicon wafer. This sample was then loaded into the same heating chamber of the MBE machine. The sample was heated to 480 °C for fifteen minutes, and it was also confirmed that no outgassing took place due to the presence of the QDs. That being ensured, the sample was, then, allowed to cool down, and removed carefully from the MBE. PL and PLE measurements was done right after, and compared with the measurements of the QDs observed prior to the heat treatment. The observations are shown in Figure 4.4.

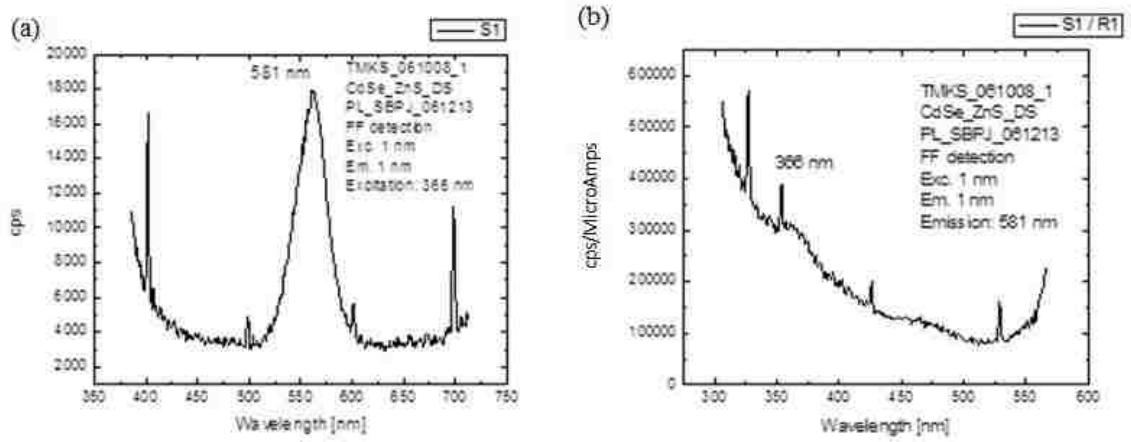

Figure 4.4: (a) and (b) PL & PLE spectra of the silicon wafers containing the QDs after they were thermally treated at 480 ºC inside the MBE.

The CdSe/ZnS QDs were excited using a wavelength of 355 nm and an intensity of 1,000,000 cps was observed before the heat treatment. The intensity dropped, by about fifty times, to 20,000 cps after the thermal treatment in the MBE. We also observed that the excitation feature occurred at 365 nm, when checked for emission at 575 nm prior to the heat treatment. After the heat treatment, the excitation feature was no longer high enough, and other peaks (lamp artifacts) could also be seen. It should be noted that the walls of the integrating sphere, which is used to measure quantum efficiency (QE), start absorbing light at around 350 nm and therefore, the 365 nm feature on the PLE spectrum was chosen as the standard excitation wavelength.

4.5. Heat treatment of the QDs at different temperatures to determine exact temperature at which they lose their photoluminescence property

Further experiments were necessary to investigate whether the QDs retained their core-shell structure, or any intermixing occurred between the two layers. This was done by annealing the QDs in a vacuum environment, at different temperatures starting from 200 °C, and measuring the PL and QE to observe any shift in the PL spectra.

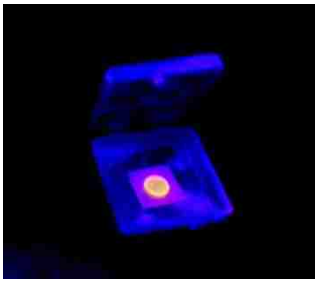

Figure 4.5: CdSe/ZnS QDs on the sapphire substrate emit around 570 nm as seen under the UV lamp.

The QDs were placed on a (1x1) cm^2 sapphire substrate, as shown in Figure 4.5. Sapphire was chosen as it is highly transparent to wavelengths of light, between 150 nm (ultraviolet) and 5500 nm (Infra-Red), and as such, it would not interfere with the PL from the QDs. PL of the bare sapphire substrate was measured, as shown in Figure 4.6(a), to verify that there was no emission from the excitation wavelength of the QDs. Next, 1.0 µl of the dots were pipetted onto the center of the sapphire substrate.

The PL at room temperature was measured, at first, to serve as a control for comparison with the PL obtained from each of the higher temperatures. The QD annealing experiments were carried out in the preparation chamber of the MBE system, in a vacuum environment, by heating them to 200 °C and increasing the temperature at steps

of 50 °C until the QDs stopped exhibiting any QE, which was found to be at 250 °C. The PL and QE were measured at each of these temperatures, as shown in Figures 4.6(b)-(c), 4.7 and 4.8.

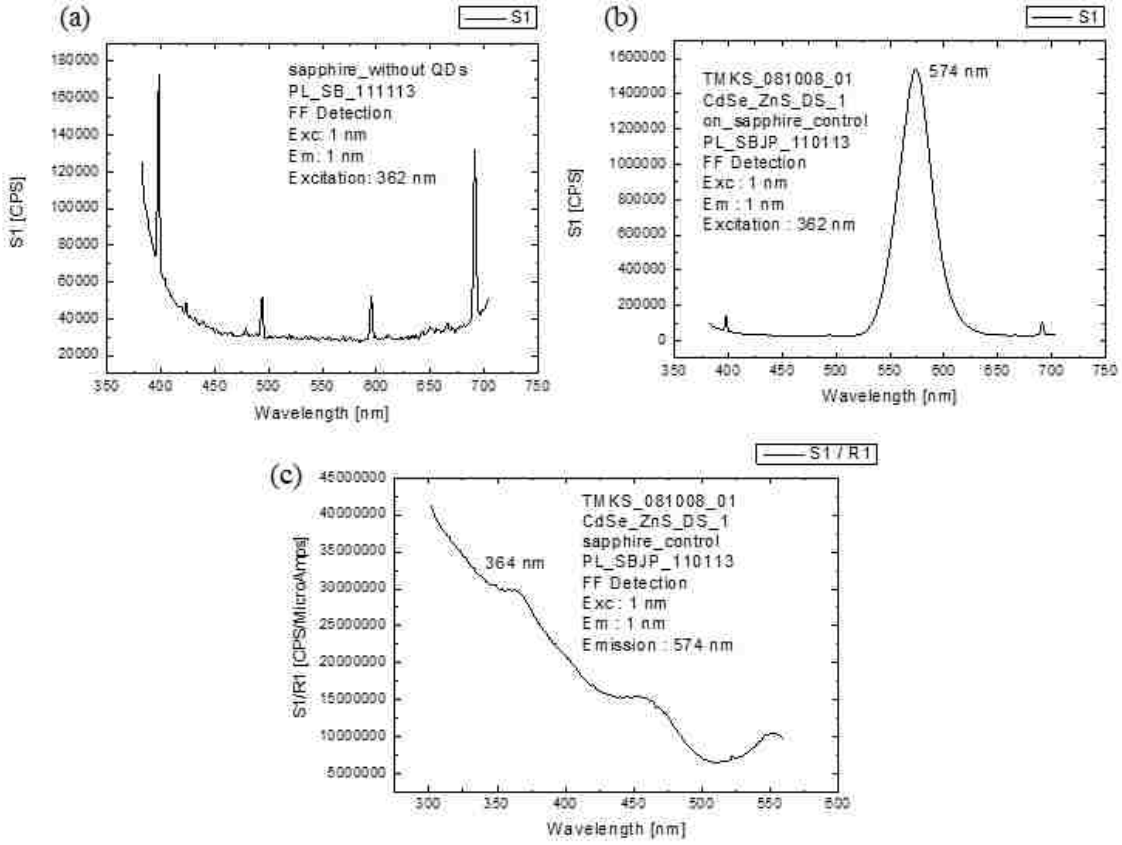

Figure 4.6: (a) PL spectra of the bare sapphire substrate which indicates no emission from 362 nm excitation (b) PL spectra of the sapphire with the CdSe/ZnS QDs at room temperature (c) PLE spectra of the sapphire with the CdSe/ZnS QDs at room temperature.

The PL spectra, as shown in Figures 4.6 (b) and (c), showed that the CdSe/ZnS QDs on sapphire emitted strongly at 574 nm, with a 1.40 million cps, for an excitation wavelength of 362 nm. When measuring the PLE using a 574 nm emission wavelength, the excitation spectrum increases in intensity well into the UV, as seen in Figure 4.6 (c). However, because the walls of the integrating sphere, which is used to measure QE, start

absorbing light at around 360 nm, the 362 nm feature on the PLE spectrum was chosen as the standard excitation wavelength.

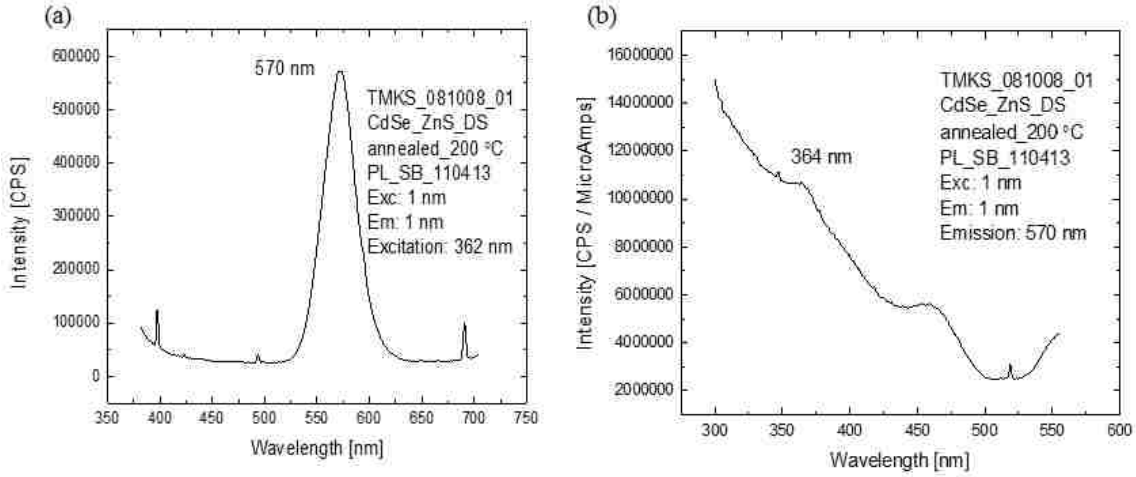

Figure 4.7: (a) & (b) show the PL and PLE spectra of the sapphire with the CdSe/ZnS QDs when heated to 200 °C in a vacuum environment inside the MBE system.

The PL spectra of the QDs annealed at 200 °C are shown in Figure 4.6. An emission peak at 570 nm was observed, for a 362 nm excitation. The intensity of the QDs decreased by 2.5 times to 0.56 million cps, at this temperature. When checked for the 570 nm emission, a PLE feature at 364 nm wavelength was observed, indicating no shift in the PL spectra.

The PL spectra of the QDs annealed at 250 °C are shown in Figure 4.8. The emission peak and excitation feature remained at 573 nm and 364 nm respectively, indicating that there was no shift in the spectra. The emission intensity, however, dropped by about 7 times to only 0.2 million cps this time.

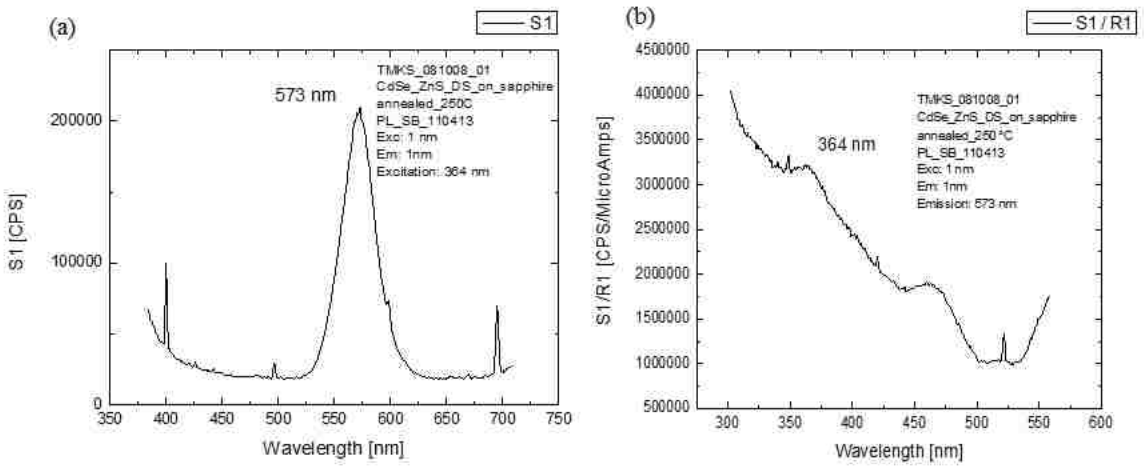

Figure 4.8: (a) & (b) show the PL and PLE spectra of the sapphire with the CdSe/ZnS QDs when heated to 250 °C in a vacuum environment inside the MBE system.

The QE at room temperature was measured, and found to be very high at 95.8 %. It decreased to about 30 % when the QDs were annealed to 200 °C. Finally, at 250 °C, the QE dropped to about 4 %. From these results, we concluded that although the CdSe/ZnS QDs did not show any core-shell intermixing at an elevated temperature of 200 °C (no shift in PL spectra was observed), the quantum dots lost their PL property at temperatures of 250 °C, and above.

4.6. Integration of the colloidal QDs into the nanovoids, optical characterization results, and analysis

Finally, 1.0 µL of the CdSe/ZnS QD solution were pipetted on to the 'nanovoid' (GaAs/GaSb) sample. The sample was etched with $NH_4OH:H_2O_2$ solution for 5 min, to selectively etch off the coalescing GaAs capping layer, and expose the GaSb nanovoids. PL measurements were performed on this sample, before and after placing the QDs. The

PL of the sample without the QDs (Figure 4.9) served as a control. It showed that there was no emission from the bare GaAs/GaSb sample when excited at 364 nm, which is the excitation wavelength measured for the QDs, as mentioned previously.

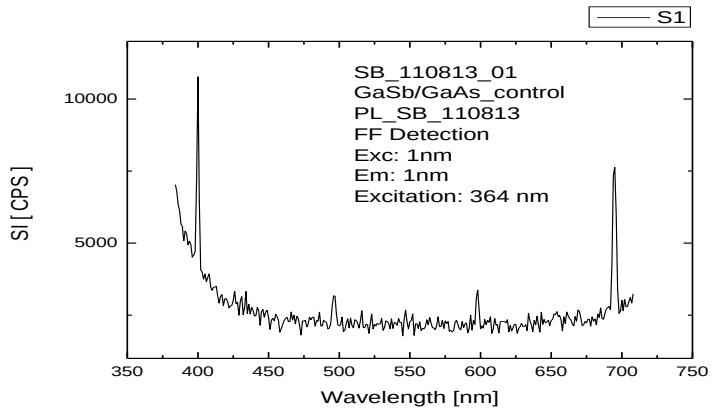

Figure 4.9: shows the PL spectra of the bare GaSb nanovoid sample. No strong emission peaks were observed from 364 nm excitation.

The PL spectra of the QDs on the GaAs/GaSb are shown in Figure 4.10. The emission peak and excitation feature were observed at 574 nm and 364 nm respectively, as expected. A strong emission intensity of 2.5 million cps was observed. This indicated that the colloidal QDs are able to fluoresce when placed on the 'nanovoid' sample. A QE of 5.3% was, however, observed as opposed to a QE of 95.8%, when the colloidal QDs were placed on sapphire. This is due to the fact that the bandgap of GaAs is high, and as such, it absorbed at the excitation wavelength of the QDs, and decreased their photoluminescence. Sapphire, on the other hand, has a wide optical transmission band (from the UV to near IR), making it highly transparent to the excitation wavelength of the QDs and thereby resulting in a stronger PL from the QDs.

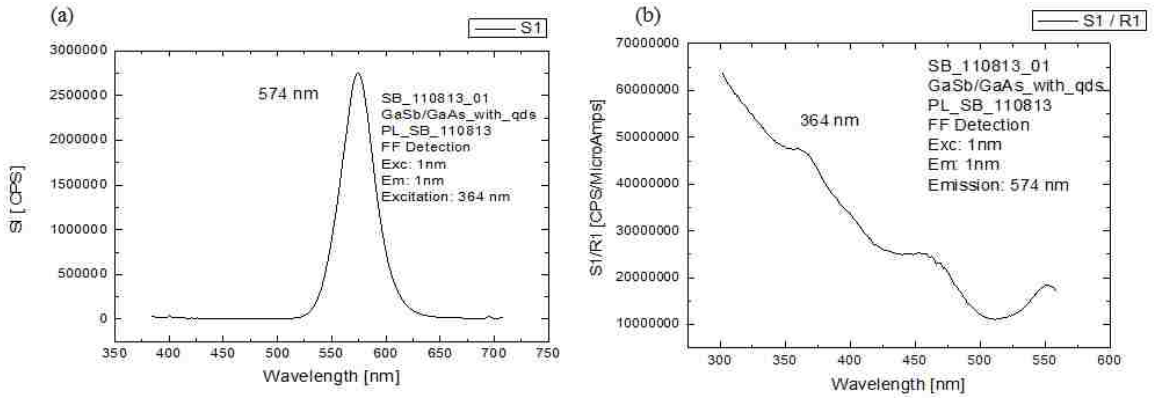

Figure 4.10: (a) and (b) show the PL and PLE spectra of the GaSb nanovoid sample with the QDs placed on it.

As the QDs were finally placed on the etched GaSb nanovoid substrate, XTEM of the sample was done to check for the integration of the CdSe/ZnS QDs with the GaSb nanovoids, as shown in Figures 4.11-4.13. A line Energy Dispersive X-ray Spectrometry (EDS) was also performed on the sample to confirm the observations. EDS makes use of the X-ray spectrum emitted by a solid sample bombarded with a focused beam of electrons to obtain a localized chemical analysis.

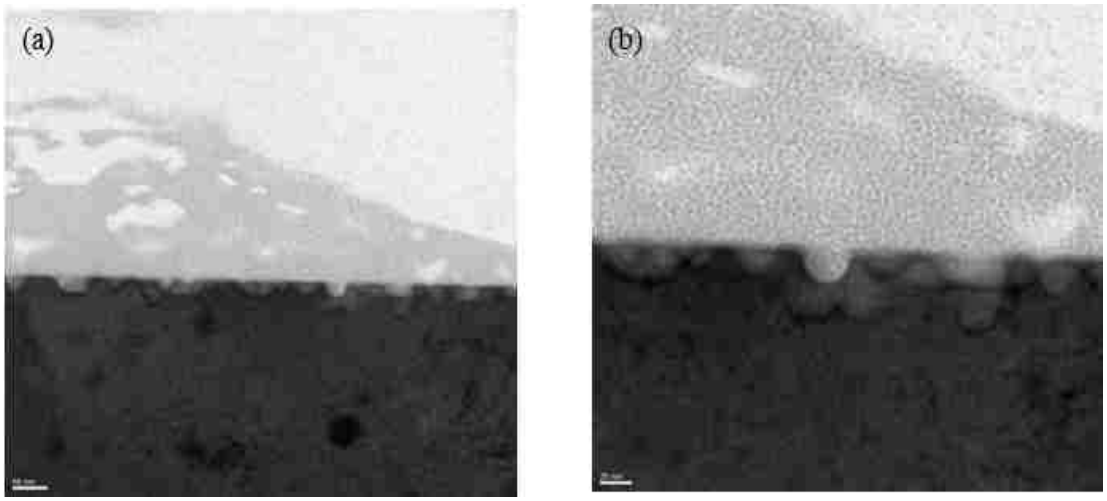

Figure 4.11: XTEM of the QDs on the GaSb nanovoid sample (R12-128) at a resolution of (a) 50 nm (b) 20 nm respectively showing the QDs on the surface as well as in the voids. All scale bars correspond to 50 nm and 20 nm respectively.

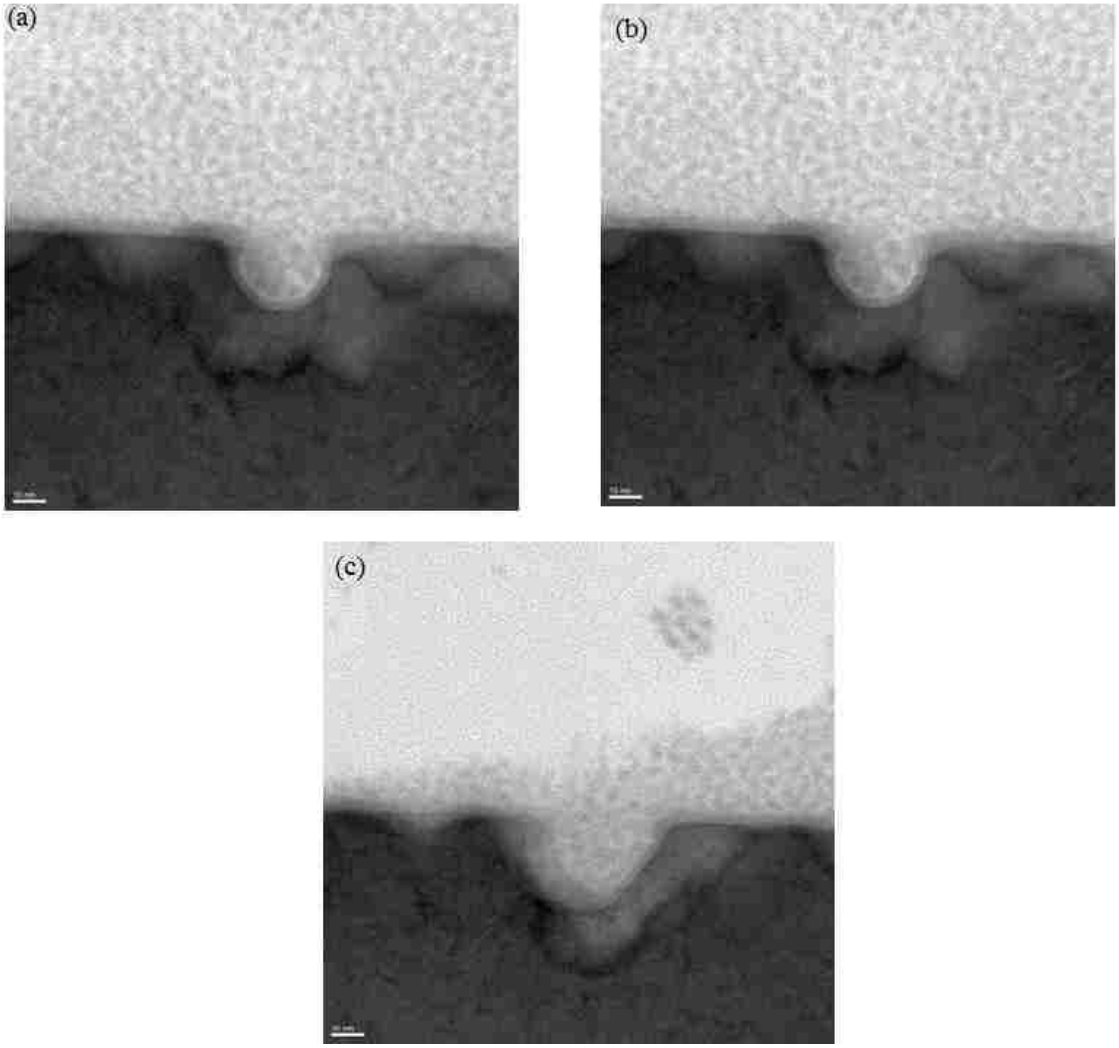

Figure 4.12: (a), (b) & (c) XTEM of the QDs on the GaSb nanovoid sample (R12-128) at a higher resolution of 10 nm. All scale bars correspond to 10 nm.

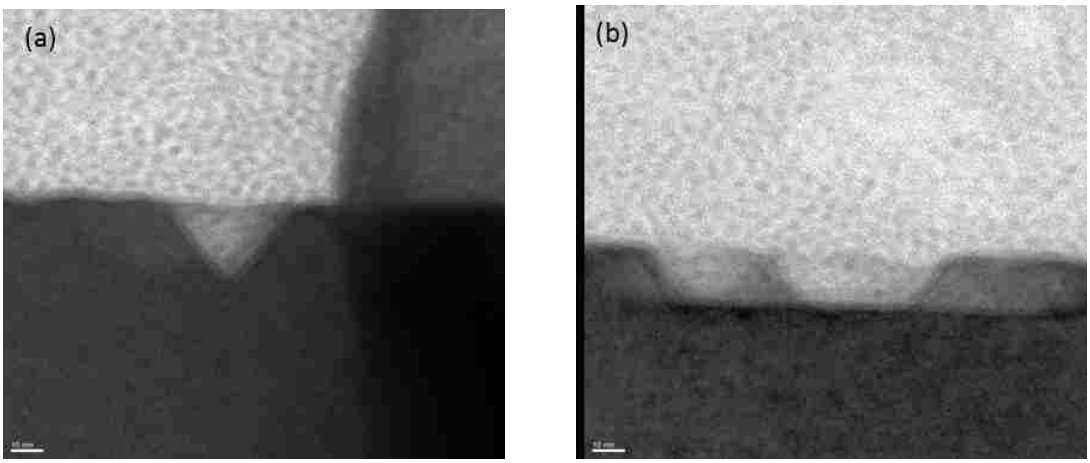

Figure 4.13: (a) & (b) XTEM on other regions of the GaSb nanovoid substrate confirming the presence of the dots in all the voids present in the sample. The gray regions in the image are the QDs as proved by EDS data (shown in next Figure). All scales bars correspond to 10 nm.

A line EDS on the nanovoid sample with the QDs showed peaks of the QD elements (Cd, Se, Zn, and S) inside the voids as shown in Figure 4.14. This proved that the QDs have been successfully placed into the nanovoids. A lot of carbon resulting from the solvent in which the QDs were suspended can be seen on the surface which needs to be removed. A capping layer can, next, be grown over the nanovoids to enclose the QDs in them.

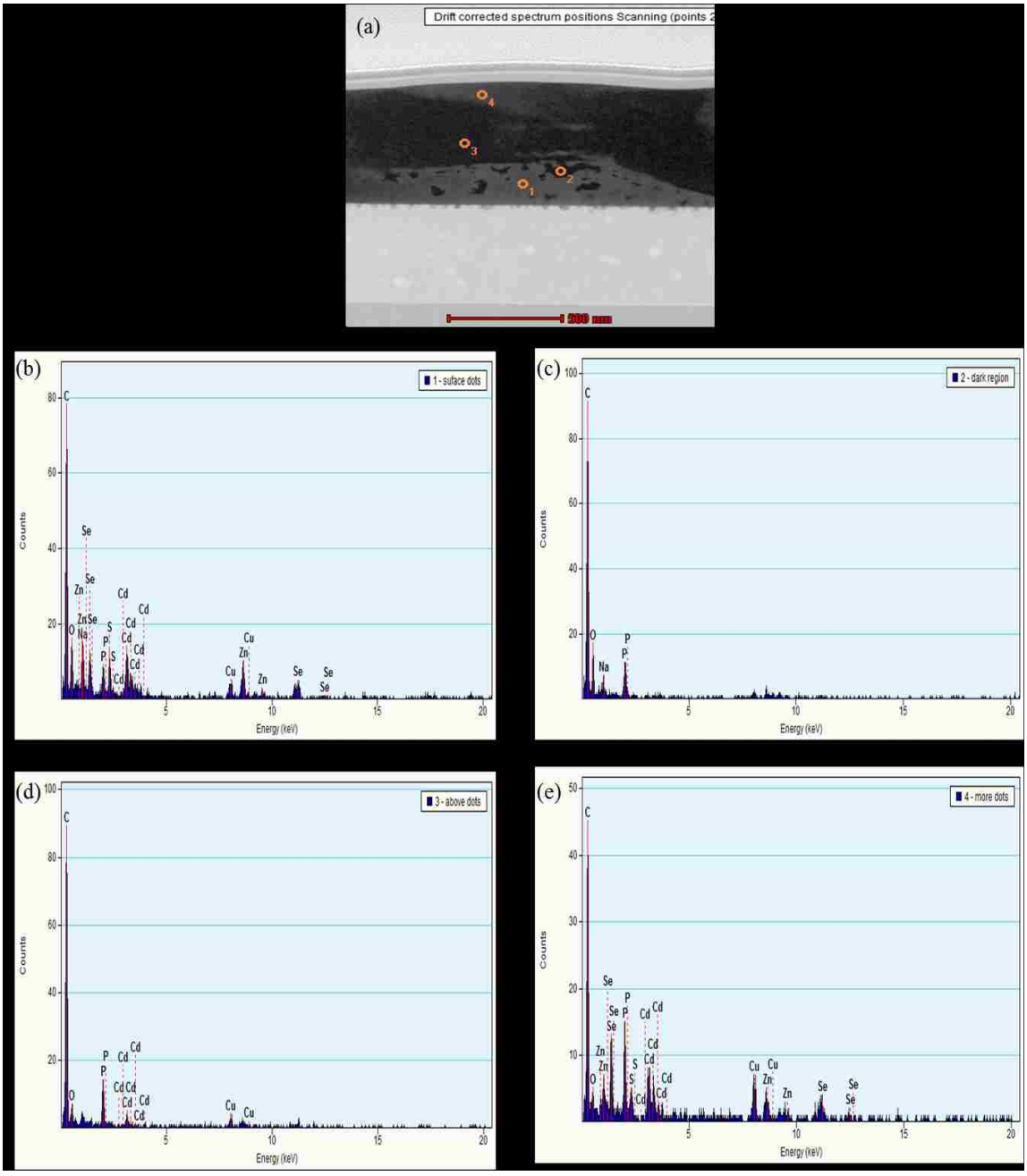

Figure 4.14: (a) TEM image showing the regions on which EDS was performed (b) EDS of region 1 showing peaks of Cd, Se, Zn and S proving the gray region to contain QDs (c) EDS of region 2 showing a C peak proving the dark regions to contain Carbon (d) & (e) EDS of region 3 and 4 respectively, showing peaks of Cd, Se, Zn and S indicating the presence of QDs on the surface.

References

Islam, M., 2010. Difference between silicon wafer <100> & <111>. URL: http://www.academia.edu/334549/Difference_between_silicon_wafer_100_and_111_ (accessed: 04 May 2014).

Seidel, H; Csepregi, L; Heuberger, A; Baumgartel, H., 1990. Anisotropic etching of crystalline silicon in alkaline solutions. J. Electrochem. Soc. 137(11), 249–260.

UCI, 2014 URL: .http://www.inrf.uci.edu/wordpress/wp-content/uploads/sop-wet-anisotropic-si-etch-using-koh.pdf (accessed: 04 May 2014).

UIUC Biosensing Inst., 2014. URL: http://nano.illinois.edu/B3SI/LabModules/MNF.pdf (accessed: 04 May 2014).

Chapter 5

Conclusion and future work

5.1. Conclusion

In this project, we have analyzed the formation and structure of the nanovoids. We have summarized the characteristics of the nanovoids, such as the surface roughness, their average dimensions, and their density using atomic force microscopy, scanning electron microscope, and transmission electron microscopy. The procedure for the synthesis of the colloidal CdSe/ZnS DS QDs was, also, summarized. Experimental procedures, PL and QE measurements of the QDs on silicon and sapphire substrates subjected to different temperatures in a vacuum environment were described, to conclude that the QDs lost their PL at temperatures of 250 °C, and above. This indicated that a capping layer of GaAs would not be possible for the nanovoids, when the QDs would be in it, as GaAs had regrowth temperatures above 500 °C. Moreover, GaAs having a higher bandgap would absorb any emission from the QDs. An alternate capping layer could be silicon dioxide, owing to its lower growth temperature. Finally, the QDs were placed on the GaAs/GaSb nanovoid sample, and were seen to still emit strongly on this surface, similar to those placed on sapphire substrate previously. Integrating the CdSe/ZnS QDs into these nanovoids was successful as confirmed by TEM and EDS data. This indicated a successful demonstration of the heteroepitaxy of dissimilar compounds (III-V and II-VI). The resulting material exhibits optical properties that may be technologically useful.

5.2. Future work

Future work in this project would involve devising a procedure to remove excess QDs from the surface of nanovoid sample. Using the solvent, hexane, to wash off the QDs, which have not been integrated into nanovoid sample, is a possible option. However, SEM, XTEM, and EDS analysis would be required to verify this process. Experiments would also need to be performed with QDs synthesized from different materials, to check if they can withstand the regrowth temperatures inside the MBE. Besides, it would be necessary to conduct experiments to find an alternative capping layer material that would be transparent to the wavelengths of light that excite the QDs integrated into the nanovoids.